AGU PUBLICATIONS

JGR

Journal of Geophysical Research: Earth Surface

RESEARCH ARTICLE
10.1002/2014JF003387

Key Points:
- Landslides are modeled using probability based on slope and precipitation
- Postglacial denudation rates decay over >100 kyr
- Response time scale of postglacial processes is longer than glacial cycles

Supporting Information:
- Text S1, Figures S1–S7, and Table S1
- Table S1

Correspondence to:
S. Moon,
sgmoon@mit.edu

Citation:
Moon, S., E. Shelef, and G. E. Hilley (2015), Recent topographic evolution and erosion of the deglaciated Washington Cascades inferred from a stochastic landscape evolution model, *J. Geophys. Res. Earth Surf.*, *120*, 856–876, doi:10.1002/2014JF003387.

Received 11 NOV 2014
Accepted 21 APR 2015
Accepted article online 24 APR 2015
Published online 22 MAY 2015

Recent topographic evolution and erosion of the deglaciated Washington Cascades inferred from a stochastic landscape evolution model

Seulgi Moon[1,2], Eitan Shelef[1,3], and George E. Hilley[1]

[1]Department of Geological and Environmental Sciences, Stanford University, Stanford, California, USA, [2]Now at Department of Earth, Atmospheric, and Planetary Sciences, Massachusetts Institute of Technology, Cambridge, Massachusetts, USA, [3]Now at Earth and Environmental Sciences Division, Los Alamos National Laboratory, Los Alamos, New Mexico, USA

Abstract In this study, we model postglacial surface processes and examine the evolution of the topography and denudation rates within the deglaciated Washington Cascades to understand the controls on and time scales of landscape response to changes in the surface process regime after deglaciation. The postglacial adjustment of this landscape is modeled using a geomorphic-transport-law-based numerical model that includes processes of river incision, hillslope diffusion, and stochastic landslides. The surface lowering due to landslides is parameterized using a physically based slope stability model coupled to a stochastic model of the generation of landslides. The model parameters of river incision and stochastic landslides are calibrated based on the rates and distribution of thousand-year-time scale denudation rates measured from cosmogenic ^{10}Be isotopes. The probability distributions of those model parameters calculated based on a Bayesian inversion scheme show comparable ranges from previous studies in similar rock types and climatic conditions. The magnitude of landslide denudation rates is determined by failure density (similar to landslide frequency), whereas precipitation and slopes affect the spatial variation in landslide denudation rates. Simulation results show that postglacial denudation rates decay over time and take longer than 100 kyr to reach time-invariant rates. Over time, the landslides in the model consume the steep slopes characteristic of deglaciated landscapes. This response time scale is on the order of or longer than glacial/interglacial cycles, suggesting that frequent climatic perturbations during the Quaternary may produce a significant and prolonged impact on denudation and topography.

1. Introduction

The topography of the Earth's surface is formed by interactions between tectonics, climate, and surface processes. Under the conditions of time-invariant rock uplift rates, climate, lithology, and surface processes, landscapes tend to approach a statistically invariant topographic form and a dynamic equilibrium between denudation and uplift rates [*Hack*, 1960; *Hergarten and Neugebauer*, 1998; *Hasbargen and Paola*, 2000; *Willett and Brandon*, 2002; *Pelletier*, 2004]. However, perturbations in tectonic rates, climate, lithology, or surface processes may create imbalances between uplift and denudation rates, and topographic features will change their forms over time [*Davis*, 1899; *Riebe et al*., 2000; *Moon et al*., 2011]. Such perturbations can be expected in a recently deglaciated landscape, where changes in climate result in an abrupt change from glacial to postglacial geomorphic processes. Previous research has studied deglaciated landscapes to examine the distribution and rates of postglacial surface processes [*Hobley et al*., 2010; *Norton et al*., 2010a, 2010b; *Moon et al*., 2011] and to understand landscape response to deglaciation [*Dadson and Church*, 2005; *Herman and Braun*, 2008]. Understanding the response of deglaciated landscapes will help to understand the impact of the periodic perturbations of climate over the Quaternary (e.g., glacial/interglacial cycles) on sediment and chemical flux to the terrestrial and marine ecosystems and the spatial distribution of steep topographic slopes. Studies have used numerical models to examine the geomorphic responses to climate and geomorphic process changes using idealized or theoretical landscapes [*Braun et al*., 1999; *Dadson and Church*, 2005], but only a few studies have modeled an actual deglaciated topography due to the difficulties in parameterizing and modeling the controls of various surface processes and limited data on landscape adjustment over millennial timescales [e.g., *Herman and Braun*, 2008].

One approach to understanding landscape adjustment to deglaciation uses geomorphic transport laws (GTLs) to formulate rates of surface lowering or sediment transport in terms of measurable metrics and

empirical parameters that can be related to topographic, climatic, ecologic, and lithologic controls [*Dietrich et al*., 2003]. GTLs of river incision and hillslope processes have been studied using field measurements, experiments, and mathematical and numerical models [*Culling*, 1960, 1963, 1965; *Howard and Kerby*, 1983; *Howard*, 1994; *Tucker and Bras*, 1998; *Roering et al*., 1999; *Whipple and Tucker*, 1999; *Stock and Dietrich*, 2003; *Perron et al*., 2009]. Landslide processes are challenging to model due to the wide variety and complexity of landslide initiation and transport [*Densmore et al*., 1998; *Dietrich et al*., 2003; *Dadson and Church*, 2005; *Booth et al*., 2013]. Since landslides are thought to be one of the dominant sediment sources in recently deglaciated landscapes [*Dadson and Church*, 2005; *Doten et al*., 2006; *Norton et al*., 2010b; *Moon et al*., 2011], it is critical to account for their role in the topographic evolution of deglaciated landscapes.

The Washington Cascades provide an excellent opportunity to model the topographic and erosional evolution of deglaciated landscapes. The Washington Cascades are currently in topographic and erosional disequilibrium after deglaciation occurred around 11–17 kyr ago [*Porter*, 1976]. The topography still shows the features inherited from prior alpine glacial processes (e.g., cirques, steep side-valleys, and flat valley bottoms), although postglacial processes are currently denuding this landscape [*Mitchell and Montgomery*, 2006]. Our previous study in this area calculated thousand-year-time scale denudation rates using cosmogenic ^{10}Be concentration (cosmogenic radionuclide (CRN)-derived denudation rates) [*Moon et al*., 2011] and showed that these rates were approximately 4 times higher than million-year-time scale uplift rates from apatite (U-Th)/He ages (A-He ages) [*Reiners et al*., 2003]. In addition, the spatial distribution of denudation rates showed a good correlation with a factor of 10 variation in precipitation across the range. We interpreted this correlation to reflect the sensitivity of landslide triggering in over-steepened deglaciated topography to precipitation, which produced high denudation rates in wet areas that experienced frequent landslides.

Based on the results of our previous study, we extend our research to examine the evolution of topography and denudation rates of the deglaciated Washington Cascades over 10^3 to 10^6 year time scales. First, we characterize postglacial denudation processes in the Cascades using a GTL-based numerical model. We propose a GTL of stochastic landslide processes, which is formulated based on a physically based slope stability model that is supplemented with a stochastic landslide generation rule. We explore two landslide rules that have different landslide depth configurations. We then calibrate the model parameters based on CRN-derived denudation rates and estimate the relative contributions of individual postglacial surface processes. The uncertainties within and covariations between model parameters are estimated using a Bayesian inversion scheme to assess the important controls of denudation rates. Finally, using current topography as an initial condition, we simulate how the topography and denudation rates evolve as the postglacial surface processes rapidly denude the deglaciated landscape. We estimate the minimum time scale of landscape response to deglaciation and discuss how cyclic glacial/interglacial variations will affect the long-term landscape evolution during the Quaternary.

We find that the calibrated model provides a satisfactory explanation of the thousand-year-time scale denudation rates, modern topography, the observed frequency of landslide generation estimated for the area, and the river incision coefficient independently estimated in similar rock types. Our model explores potential ranges of response time scales of denudation rates after deglaciation. The minimum response time scale of denudation rates in the deglaciated Cascade Mountains varies from 100 to 960 kyr, which is on the order of or longer than the recent recurrence of deglaciation. This study shows that such a landscape evolution model can provide insight into the time scale of landscape response and temporal evolution of topography due to glacial/interglacial cycles.

2. Methods

2.1. Data Sources

We modeled a region of the Cascades that extends 140 km from N to S and 130 km from E to W (Figure 1). Topography was represented by a 100 m resolution digital elevation model (DEM) downsampled from 30 m resolution National Elevation Dataset DEM. Mean annual precipitation (MAP) with 800 m resolution was acquired from the PRISM data set for 1971–2000 [*PRISM*, 2006] and resampled to the same 100 m resolution grid. Drainage area and slope were calculated based on a D8 flow routing scheme, and the discharge was calculated from the distribution of precipitation using the same scheme [*O'Callaghan and*

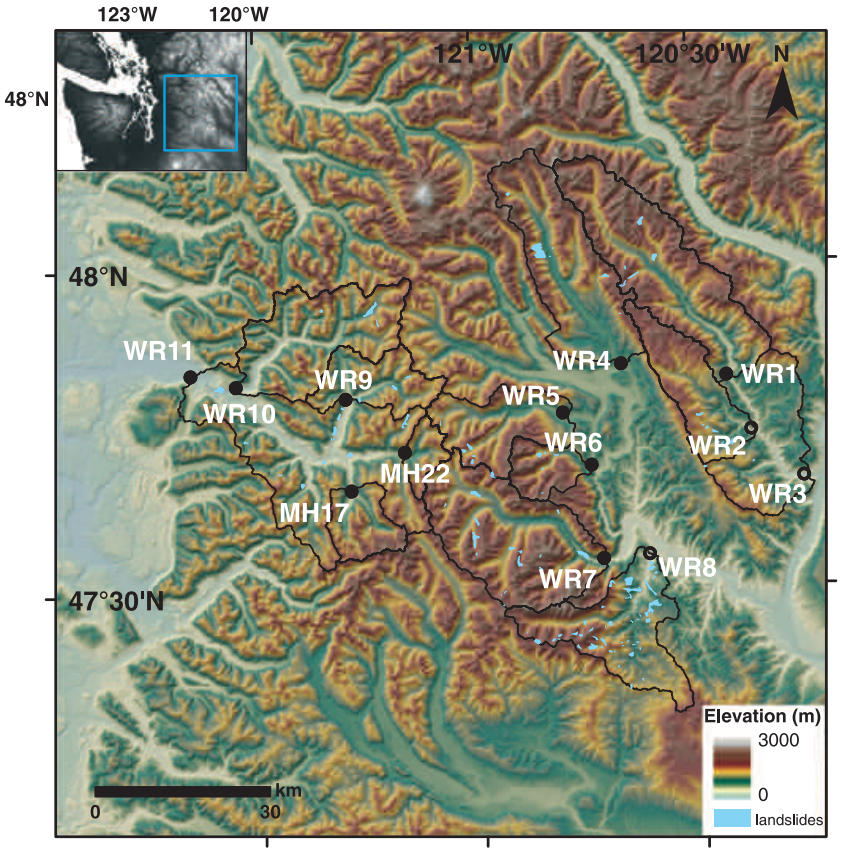

Figure 1. Map of study area. The locations of 13 basins with CRN-derived denudation rates are shown as black circles, and their drainage areas are shown by black lines. The open circles indicate partially glaciated basins whose area was less than 75% glaciated during LGM. The areas of current landslide inventories within our basins are shown in pink [*Boyd and Vaugeois*, 2003].

Mark, 1984; *Pelletier*, 2010; *Shelef and Hilley*, 2013]. The D8 flow routing scheme was used to calculate flow paths and contributing areas, principally because it is preferable when the DEM resolution is coarse (i.e., 100 m DEM) relative to a typical channel width and/or hillslope length [*Shelef and Hilley*, 2013] (see supporting information for details). Million-year-time scale uplift rates were assumed to be equal to million-year-time scale exhumation rates inferred from A-He ages based on the assumption that mountain relief has been similar since 8–15 Ma in the Cascades [*Takeuchi and Larson*, 2005]. Bedrock A-He ages in this region ranged from 4.4 Ma to 60 Ma, which corresponds to exhumation rates ranging from 0.01 to 0.33 mm/yr [*Reiners et al*., 2002, 2003]. The spatial distribution of uplift rates was interpolated using a Simple Kriging method allowing 100% measurement errors and smooth neighborhood interpolation (Figure S1 in the supporting information). The smooth interpolation was applied with a large measurement error (100%) to minimize the biases from outliers and to allow a smoothly extrapolated surface within the extent of our study region. Clustering of A-He samples caused uplift rates that were interpolated over the studied region to be less than those obtained from point measurements, which ranged from 0.03 to 0.20 mm/yr (Figure S1 in the supporting information). CRN-derived denudation rates from 13 basins across the Cascades ranged from 0.08 to 0.57 mm/yr, representing average denudation rates over 1.1–7.4 kyr [*Moon et al*., 2011].

2.2. Landscape Evolution Model

We model postglacial surface processes of the deglaciated Washington Cascades using a GTL-based numerical model [*Howard*, 1994; *Dietrich et al*., 2003; *Shelef and Hilley*, 2013]. This section describes the structure of the model, while the impacts of the model assumptions made here are discussed in section 4.1. The model includes bedrock uplift, sediment transport by linear diffusion, detachment-limited

Table 1. Model Parameters

		A Priori		*Scenario SD: A Posteriori*					*Scenario SS: A Posteriori*			
		Min	Max	SD1 Best Fit[a]	SD2 Second Best Fit[a]	95% CI (χ^2_{adj})	95% CI (χ^2_{meas})		SS1 Best Fit	95% CI (χ^2_{adj})	95% CI (χ^2_{meas})	
Soil diffusion												
D	($m^2\,yr^{-1}$)	0.0035	0.0035	**0.0035**	**0.0035**				**0.0035**			
River incision												
K_d	($m^{1-2\,m}\,yr^{-1}$)	1.0×10^{-9}	1.0×10^{-5}	$\mathbf{1.0\times10^{-6}}$	$\mathbf{1.0\times10^{-6}}$	1.0×10^{-7}	2.0×10^{-6}	5.0×10^{-7}	1.0×10^{-6}	$\mathbf{1.0\times10^{-9}}$	4.0×10^{-8}	2.0×10^{-6}	6.3×10^{-9}	4.0×10^{-7}
m		0.5		**0.5**	**0.5**					**0.5**				
n		1		**1**	**1**					**1**				
Stochastic landslides														
T	($m^2\,yr^{-1}$)	3.2×10^{1}	3.2×10^{3}	$\mathbf{1.1\times10^{3}}$	$\mathbf{0.9\times10^{3}}$	4.0×10^{2}	2.8×10^{3}	5.6×10^{2}	2.0×10^{3}	$\mathbf{1.3\times10^{3}}$	2.8×10^{2}	2.8×10^{3}	8.9×10^{2}	2.8×10^{3}
P_{max}	($m^{-2}\,yr^{-1}$)	5.0×10^{-11}	5.0×10^{-6}	$\mathbf{4.0\times10^{-9}}$	$\mathbf{2.5\times10^{-8}}$	2.0×10^{-9}	2.5×10^{-7}	1.0×10^{-8}	1.0×10^{-7}	$\mathbf{2.5\times10^{-6}}$	2.5×10^{-8}	2.5×10^{-6}	4.0×10^{-7}	2.5×10^{-6}
FI_{max}		1	30	**1**	**12**	5	29	5	29	**29**	5	29	5	29
FI_{min}		0.5		**0.5**	**0.5**					**0.5**				
$P_{FI=1}$				$\mathbf{4.0\times10^{-9}}$	$\mathbf{1.1\times10^{-9}}$	5.6×10^{-10}	7.1×10^{-9}	5.6×10^{-10}	2.2×10^{-9}	$\mathbf{4.4\times10^{-8}}$	5.6×10^{-9}	7.1×10^{-8}	3.5×10^{-8}	5.6×10^{-8}
S_0	(°)	0.3	1	**1**	**0.9**	0.5	0.9	0.6	0.9	**1**	0.4	0.9	0.9	0.9
b	(m)	100	100	**100**	**100**					**100**				

[a]Numbers in bold indicate the best fit parameters from the exhaustive search, and numbers in italic indicate fixed parameters.

channel incision, and surface lowering by stochastic landslide processes. The elevation change due to these processes can be expressed as

$$\frac{dz}{dt} = U + \nabla\cdot(DS) - K_d A^m S^n - \eta_{ls} \quad (1)$$

where z is surface elevation (L) and t is time (t). The U term on the right-hand side represents vertical uplift rate of rock relative to sea level ($L\,t^{-1}$). The second term represents surface lowering due to sediment transport by linear diffusion, which is expressed as a function of surface gradient (S) and a spatially constant diffusivity coefficient D ($L^2\,t^{-1}$) [*Culling*, 1960, 1963, 1965]. The third term represents detachment-limited channel incision. Based on either channel-bed shear stress or stream power, channel incision rate can be expressed as a function of the local channel slope (S), upstream contributing area (A (L^2)), erosional efficiency (K_d ($L^{1-2\,m}\,t^{-1}$)), and empirical constants of m and n whose ratio (m/n) is commonly close to 0.5. The K_d is affected by various factors such as rock erodibility, precipitation, sediments, and hydraulic geometry [*Howard and Kerby*, 1983; *Seidl and Dietrich*, 1993; *Howard*, 1994; *Whipple and Tucker*, 1999]. The last-term, η_{ls} ($L\,t^{-1}$), represents the surface lowering by stochastic landslide processes, which are likely affected by rock properties, precipitation, vegetation, and local slopes [*Dadson and Church*, 2005].

The stochastic landslide process is based on the assumption that our model cannot predict the exact location of landslides but can predict the spatial distribution of the relative propensity of slope failure [*Montgomery and Dietrich*, 1994; *Dadson and Church*, 2005]. Our stochastic landslide model is motivated by *Dadson and Church* [2005], who modeled the postglacial topographic evolution of an idealized glaciated valley using stochastic process of deep-seated (bedrock) landslides. This model triggered landslides randomly from a subset of topographic grid cells whose multiplication of local slope and elevation exceeded a critical value. Similarly, we also treat landslide processes as stochastic. However, we trigger landslides using a probability based on the spatial distribution

of topographic slopes and degree of saturation of the near-surface layer, which together conspire to produce spatial and temporal variations in pore pressures that ultimately aid in landslide failure.

The modeling of stochastic landslides consists of three parts: (1) assessing slope instability, (2) relating slope instability to the probability of failure, and (3) determining landslide depth and volume of the failure. First, we calculate the spatial distribution of slope instability using a topographic metric called failure index (FI). The FI is calculated from the spatial distributions of precipitation and topography and is analogous to the inverse of the factor of safety. Higher values of FI represent increasing slope instability. The FI value is calculated from a version of the infinite slope approximation for the failure of a cohesionless frictional material, which is coupled to a steady state hydrologic model [*Montgomery and Dietrich*, 1994; *Moon et al*., 2011].

To calculate FI for each topographic grid cell (in our study, 100 m × 100 m), we first calculate a wetness value (hereafter, *W*). *W* represents the ratio between the hydraulic flux at a given precipitation relative to that at the saturated soil [*Montgomery and Dietrich*, 1994]:

$$W = \frac{qA}{bT\sin\theta} \tag{2}$$

where *W* is allowed to vary from 0 (unsaturated) to 1 (completely saturated), *q* is the steady state precipitation during a specific storm event ($L\,t^{-1}$), *A* is the contributing area (L^2) draining across the contour length *b* (L), *T* is the saturated soil transmissivity adjusted for porosity (hereafter, transmissivity *T* ($L^2\,t^{-1}$)), and θ is the local slope in radians. We use the grid element size for *b* (i.e., 100 m), calculate θ from topographic slope, and use a constant value of *T* (Table 1). This model assumes steady state precipitation, which is not always achieved during a typical storm (as such, it does not capture the transient hydrology that is demonstrably important for triggering individual slope failures [*Iverson*, 2000]). To represent the spatial distribution of steady state precipitation (*q*) for a storm event in the model, we use the spatial distribution of mean annual precipitation (MAP) averaged between 1971 and 2000 [*PRISM*, 2006].

Based on a calculated wetness value, we calculate FI for the topographic grid cell as

$$\mathrm{FI} = \frac{S}{S_0}\left(1 - W\frac{\rho_w}{\rho_s}\right)^{-1} = k(W)\frac{S}{S_0} \tag{3}$$

where S_0 is the threshold slope that is the internal angle of friction of cohesionless material, *S* is the local slope (tan θ), ρ_s is the wet bulk density of soil (2.0 g/cm^3), and ρ_w is the bulk density of water (1.0 g/cm^3). The equation can be simplified in the form of local slope, threshold slope, and a variable *k*(*W*), assuming no cohesion of the failed material. The *k*(*W*) varies from 1 to 2, which represents the degree to which landslides are promoted by increased pore pressure.

Coupling the steady state hydrologic model to the slope stability model provides an assessment of the relative propensity for slope failure but does not directly provide the timing of landslides because the steady state assumption of the landslide model excludes time dependence. We introduce a time scale into this analysis by assuming that increasing slope instability likewise increases landslide frequency [*Reid*, 1998; *Griffiths and Fenton*, 2004; *Turner et al*., 2010]. Based on FI, we calculate the rate of failure per unit area of ground surface (landslides $L^{-2}\,t^{-1}$) (hereafter, failure density, abbreviated to *P*), assuming a modeled relationship with FI (Figure 2). After integrating the failure density over the grid cell size, we can calculate the yearly probability that this grid cell will fail (hereafter, failure rate (landslides t^{-1})), similar to landslide frequency.

The surface lowering by discrete landslides can be expressed as

$$\eta_{ls} = P(\mathrm{FI})\cdot(\Delta x\ \Delta y)\cdot d \tag{4}$$

$$P = \begin{cases} P_{\min} & \text{if} \quad \mathrm{FI} < \mathrm{FI}_{\min} \\ \dfrac{P_{\max} - P_{\min}}{\mathrm{FI}_{\max} - \mathrm{FI}_{\min}}\cdot(\mathrm{FI} - \mathrm{FI}_{\min}) & \text{if} \quad \mathrm{FI}_{\min} < \mathrm{FI} < \mathrm{FI}_{\max} \\ P_{\max} & \text{if} \quad \mathrm{FI} > \mathrm{FI}_{\max} \end{cases}$$

where *P* is the failure density, which is a function of FI; $\Delta x\Delta y$ is the unit area of a topographic grid cell in the model; and *d* is the thickness of landslide material. The relationship between *P* and FI is implemented based on a piecewise linear function that assumes a minimum failure density ($P_{\min}$) at a minimum failure index ($\mathrm{FI}_{\min}$) and a maximum failure density ($P_{\max}$) at a maximum failure index ($\mathrm{FI}_{\max}$) (Figure 2). This linear relationship is similar

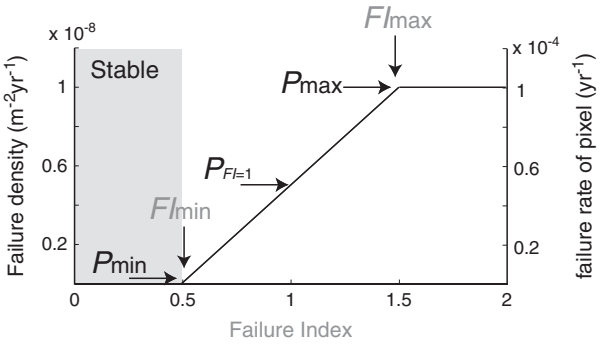

Figure 2. Modeled relationship between failure density (P) and failure index (FI). The assumed relationship between P and FI is implemented as a piecewise linear function with a minimum failure density (P_{min}) at a minimum failure index (FI_{min}) and a maximum failure density (P_{max}) at a maximum failure index (FI_{max}). $P_{FI=1}$ represents failure density at the point of failure (FI = 1). The example of modeled relationship is shown for $FI_{min} = 0.5$, $FI_{max} = 1.5$, and $P_{min} = 0\ m^{-2}\ yr^{-1}$, $P_{FI=1} = 0.5 \times 10^{-8}\ m^{-2}\ yr^{-1}$, and $P_{max} = 10^{-8}\ m^{-2}\ yr^{-1}$. The FI_{min} and P_{min} are assigned, and P_{max} and FI_{max} can be calibrated based on CRN-derived denudation rates (see section 2.3). The secondary y axis on the right shows the corresponding failure rate over a topographic grid cell (100 m × 100 m).

to the inverse relationship between failure probability and factor of safety in *Griffiths and Fenton* [2004]. We assume that P_{min} is zero at FI_{min} of 0.5 (factor of safety of 2). The FI_{min} is intended to represent the stable conditions that may not generate landslides [*Turner et al.*, 2010]. FI_{max} and P_{max} are free parameters, which are calibrated based on Bayesian approach described in section 2.3.

The landslide thickness d is measured from the surface to the failure plane, which in our model can extend into the bedrock or be fixed at the soil-bedrock interface. We test two scenarios based on these assumptions. The first scenario assumes that the failure plane extends deep into the bedrock. Hereafter, we refer this scenario as SD. The landslide thickness d for each grid node is calculated from elevation difference produced by the slope adjustment (Figure S2a in the supporting information). We assume that a landslide will lower the topographic slope to the maximum stable slope S_f, which varies with the degree of saturation. For the condition of instability (FI = 1), S_f is equal to $S_0/k(W)$ (equation (3)). We define the landslide thickness d as

$$d = \left(S - \frac{S_0}{k(W)}\right)\delta x \tag{5}$$

where δx will be Δx in the N-S and E-W directions and $\sqrt{2}\Delta x$ in the NE-SW and NW-SE directions when $\Delta x = \Delta y$. We did not assign a fixed S_f, because a statewide landslide inventory shows that the slopes of 118 landslides in our basins vary: the mean slopes along landslides varies from 0.08 to 0.64 (interquartile range of 0.28–0.42), and the maximum slopes vary from 0.1 to 0.95 (interquartile range of 0.47–0.65) (Figure S2b in the supporting information) [*Boyd and Vaugeois*, 2003].

In the second scenario, we assume that the failure plane is located at a fixed depth of 1 m, which we regard as an approximate soil depth in the area [*Schmidt et al.*, 2001; *Doten et al.*, 2006; *Hren et al.*, 2007]. This scenario assumes a specific landslide depth, and we refer this scenario as SS. We acknowledge that the soil depth in the Cascades varies spatially—our scenario-based approach is intended to provide broad constraints on the end-member modes of slope failure that plausibly occur within this landscape. Therefore, we do not include landslide rules with different thickness configurations as independent GTLs. Instead, we examine the impact of these assumptions on our results, particularly the potential ranges of model parameters and response time scales (section 4.3).

Landslides are generated based on failure probability deduced from a failure function between FI and failure density relationship (Figure 2). In scenario SD, a topographic grid cell with FI > 1 has a landslide thickness greater than zero. So landslides will occur in the cells with FI > 1. In scenario SS, a topographic grid cell with FI > 0.5 is subject to failure. We calculate the expected landslide denudation rate at each grid cell due to landslides, by multiplying the failure rate, the integrated failure density over a grid cell size, with the thickness of landslide material (d). These rates represent the statistically averaged denudation rates from landslides over a time scale longer than landslide recurrence intervals. These averaged denudation rates are used to calibrate model parameters (section 2.3). The implementation of stochastic landslides for a given time step in the landscape evolution model is explained in section 2.4.

2.3. Calibration of Model Parameters

Using the landscape evolution model described above, we calculate denudation rates from postglacial processes including hillslope transport, river incision, and stochastic landslides. According to our previous

study, basin-averaged denudation rates from cosmogenic ^{10}Be over 1.1–7.4 kyr time scales varied by a factor of ~7 across the Washington Cascades [*Moon et al*., 2011]. Our previous study showed that the spatial distribution of FI corresponded to those of enhanced denudation rates, which suggests that landslide processes likely contribute significantly to denudation rates. Other studies in deglaciated landscapes also suggest that landslide processes will be the dominant sediment source [*Dadson and Church*, 2005; *Doten et al*., 2006; *Norton et al*., 2010b]. Considering that the Cascades is occupied mostly by steep slopes and has relatively thin soils (<2 m) [*Doten et al*., 2006; *Hren et al*., 2007], we assume that hillslope transport processes by linear diffusion will be a relatively minor contributor to the measured denudation rates relative to landslide processes. Therefore, instead of optimizing soil diffusivity, we used the constant D of 0.0035 m^2/yr, which is an averaged soil diffusivity from Oregon Coast Range in Pacific Northwest [*Reneau and Dietrich*, 1991].

Under these assumptions, we calibrate the model parameters for river incision processes and stochastic landslides using the spatial distribution and magnitude of CRN-derived denudation rates. We examine the ranges of modeled denudation rates by exploring model parameters using an exhaustive search method. By comparing modeled with CRN-derived denudation rates, we find the best fit parameters and quantify the uncertainties of model parameters using Bayes' theorem [*Bayes*, 1763]. The Bayesian approach views the model parameter as a joint probability density function (pdf) whose dimension corresponds to the number of model parameters. In this approach, we can construct a joint probability density function of model parameters based on misfit between model and observed data set. This joint pdf allows examining uncertainties within and covariations between model parameters and informing the combination of the model parameters that produce comparable fit to observed data set. The statistical approaches using Bayes' theorem such as brute-force, Metropolis-Hastings, and Markov-Chain Monte Carlo algorithms have been applied to geomorphic studies to calibrate parameters in experiments and numerical models [*Vrugt et al*., 2003; *Hilley et al*., 2010; *Hobley et al*., 2011; *Pelletier et al*., 2011]. We adopt the procedure described in *Hilley and Young* [2008a, 2008b] and *Hilley et al*. [2010] but implement brute-force exhaustive sampling instead of Metropolis-Hastings Markov-Chain Monte Carlo sampling method.

Based on the spatial distribution of precipitation and topography, we calculate the expected denudation rates from river incision and stochastic landslides in the study area by varying five model parameters (K_d, T, $P_{\max}$, $\mathrm{FI}_{\max}$, and S_0) in equation (1). We varied K_d, $P_{\max}$, and T by 4, 5, and 2 orders of magnitude with an equal interval in log space 0.1, 0.1, an 0.05, respectively. We varied $\mathrm{FI}_{\max}$ from 1 to 30 with an interval of 1 and varied S_0 from 0.3 to 1 with an interval of 0.1. The ranges of K_d and T are selected to encompass the variations in previous studies [*Montgomery and Dietrich*, 1994; *Stock and Montgomery*, 1999], the maximum $\mathrm{FI}_{\max}$ is calculated from current topography, S_0 is obtained from landslide inventories (Figure S2b in the supporting information), and the maximum $P_{\max}$ is calculated considering spatial and temporal scales of the model (see supporting information). In sum, we examined >20 million combinations of the five model parameter ($41 \times 41 \times 51 \times 30 \times 8$) (Table 1). For each combination of the assigned model parameters, we calculate the goodness of model fit using a weighted-residual sum of square errors (WRSS) between expected denudation rates and CRN-derived denudation rates:

$$\mathrm{WRSS} = \sum_{i=1}^{n_b} \left(\frac{\varepsilon_i^{\mathrm{meas}} - \varepsilon_i^{\mathrm{pred}}}{\sigma_i^{\mathrm{meas}}} \right)^2 \tag{6}$$

where $\varepsilon_i^{\mathrm{meas}}$ is the CRN-derived denudation rate for basin i and $\varepsilon_i^{\mathrm{pred}}$ is the expected denudation rate for basin i from GTLs with a given set of parameters, σ_i^{meas} is the uncertainty in CRN-derived denudation rate, and n_b is the total number of basins. The combination of the best fit parameters is identified from the minimum WRSS (Table 1).

To examine the uncertainties within model parameters and the covariations between them, we estimate the joint probability distribution of five parameters using Bayes' theorem [*Bayes*, 1763; *Hilley and Young*, 2008a, 2008b; *Hilley et al*., 2010]. Based on Bayes' theorem, we can calculate the a posteriori probability density function (pdf) of the model parameters $P(m|x)$, the conditional probability of the model parameters that are taken into account by observation data sets. We calculate $P(m|x)$ as

$$P(m|x) = \frac{P(x|m)P(m)}{\sum_{j=1}^{n_p} P\left(x|m_j\right)P\left(m_j\right)} \tag{7}$$

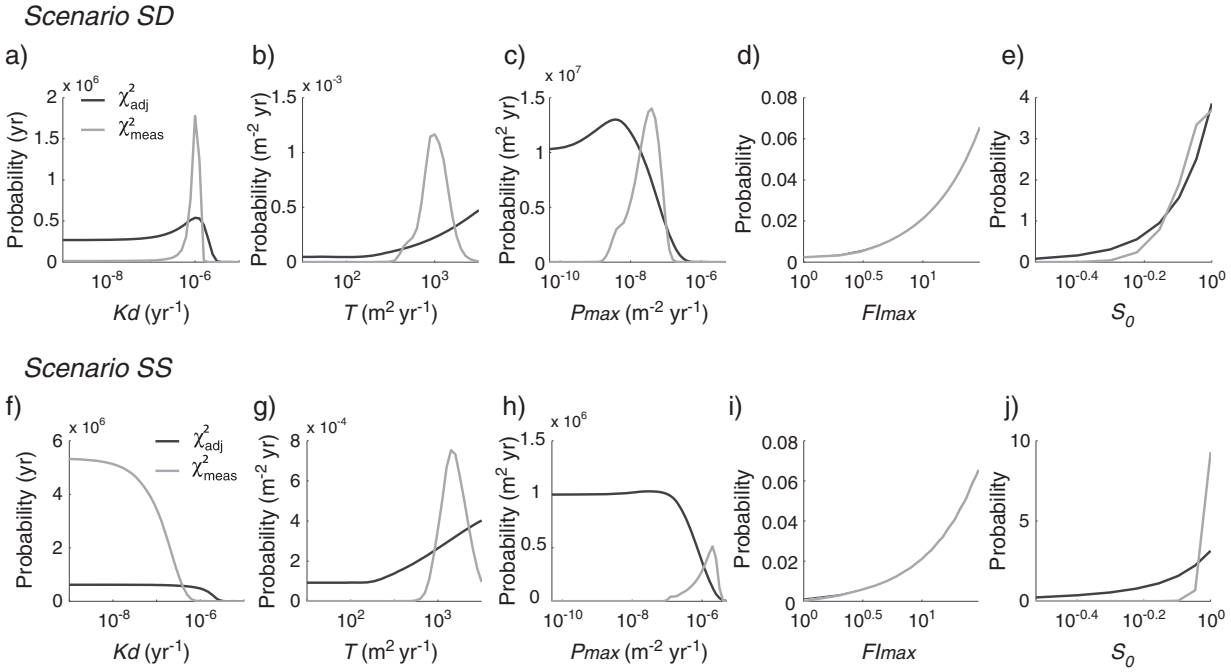

Figure 3. Marginal probability density functions of model parameters from model scenarios with different landslide depth configurations (SD and SS). In each panel, the solid line denotes the a posteriori probability density function calculated from χ^2_{adj}, and the gray line denotes those from χ^2_{meas}. The *x* axes are shown in log space. The marginal pdf for each parameter is calculated by integrating the conditional probabilities of four other dimensions except for the parameter of interest.

where *x* is a set of measured data (i.e., CRN-derived denudation rates), *m* is a set of model parameters, n_p is the total number of model parameters, and $P(x|m)$ is the probability of data given the parameter values. $P(m)$ is the a priori probability of parameters; the probability of parameters before the observational data are taken into account. We assume a uniform distribution of the a priori probability within minimum and maximum range of parameter values that are physically plausible. Then, we compare the a posteriori probability ranges of model parameters with estimates from other studies. The probability of the data given the model parameters, $P(x|m)$, is calculated as

$$P(x|m) = \exp(-\chi^2) \tag{8}$$

where the reduced chi-square value (χ^2) is calculated from WRSS divided by degrees of freedom n_f (i.e., $n_f = 8$ from 13 CRN-derived denudation rates and five free parameters). When χ^2 is close to 1, it means that misfit of the model lies within the uncertainties of the measurements. For each combination of parameters, we calculate expected denudation rates using GTLs, WRSS, and χ^2 using equation (6), the discrete probability density of $P(x|m)$ using equation (8), and then a posteriori probability distributions of the model parameters $P(m|x)$ using equation (7). The a posteriori pdf has five dimensions, which is difficult to visualize. So we construct the marginal pdf for each parameter (Figure 3) and two-dimensional joint pdfs (Figure 4) by integrating the conditional probabilities of all other dimensions except for the parameter dimension of interest.

The a posteriori probability distribution of parameters will vary depending on the choice of the uncertainties, σ^{meas}, in the χ^2 calculation. We can use the uncertainties of CRN-derived denudation rates from accelerator mass spectrometry measurements as σ^{meas} to calculate χ^2 (hereafter, χ^2_{meas}). However, previous studies showed that CRN-derived denudation rates can vary by a factor of 2 due to stochastic mass wasting events [*Niemi et al.*, 2005; *Kober et al.*, 2012]. This suggests that the uncertainties of CRN-derived denudation rates from infrequent sampling could be much larger than analytical uncertainties. In addition, our numerical model has uncertainties, since it is based on a myriad of simplifying assumptions, such as that of spatially uniform lithology and constant parameters of *D*, K_d, and *T*. These simplifying assumptions and limitations make it difficult for the model to explain the full variation of CRN-derived denudation rates. In this regard, we can conceptualize σ^{meas} as an overall model inaccuracy, which includes the potential

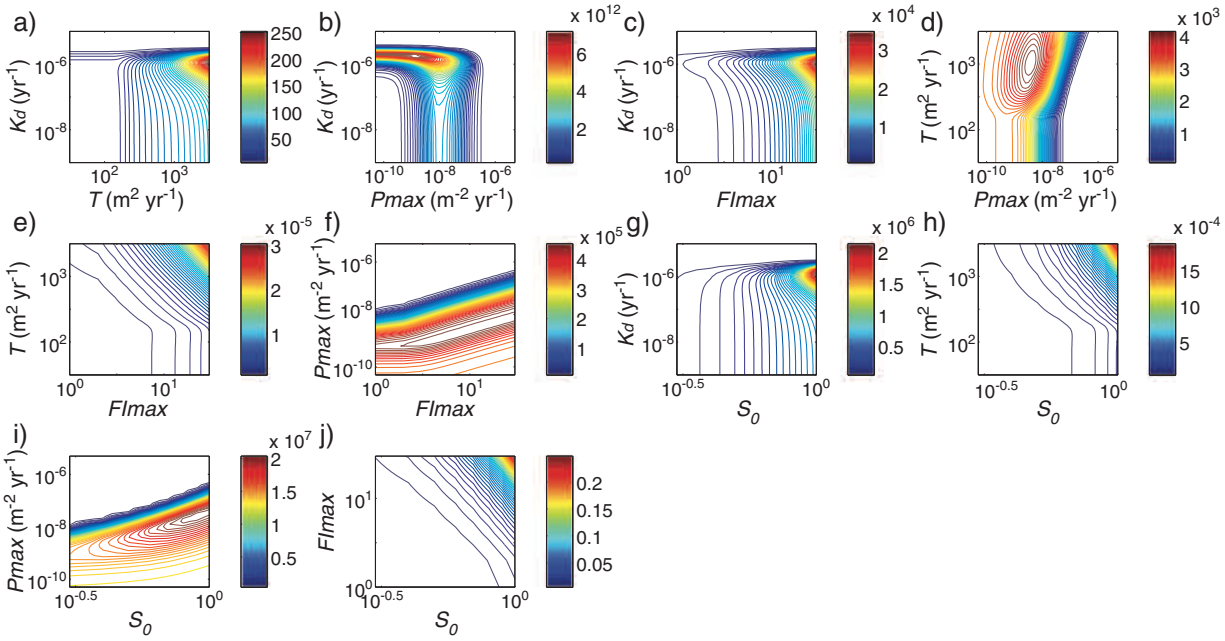

Figure 4. Two-dimensional joint probability density functions of model parameters from scenario SD. Each panel shows the a posteriori probability density distribution for two parameters calculated from χ^2_{adj}. The two-dimensional joint probability is calculated by integrating the conditional probabilities of the other three dimensions except for the parameter dimensions of interest. Both axes are shown in log space, and warm colors represent high joint probability. The extent of both *x* and *y* axes covers the full a priori range of the model space.

uncertainties in samples of CRN-derived denudation rates and the model uncertainties due to simplified assumptions and limitations. We refer the calculated χ^2 based on adjusted σ^{meas} to χ^2_{adj}.

2.4. Numerical Simulation

Based on the best fit parameters for river incision and stochastic landslides, we simulate the topographic evolution of the Cascades over time. Using current topography as an initial condition, we let surface processes modify and be modified by topography during the model simulation. Since the Cascades lies along a north-south axis and the rivers drain to the east or west, we use no flow and zero-flux boundaries for N and S and open boundaries for E and W through which water and sediment freely flow. We use a finite volume method to solve equation (1) and integrate the equation forward in time using forward Euler method. We run the model for 1 Myr with a fixed time step of 100 yr. We modify the topography using hillslope diffusion and river incision processes first and then apply the stochastic landslide rule in each time step. For hillslope diffusion and river incision processes, we add the changes of elevation to the elevation values in the previous time step for all grid points. For stochastic landslides, we modify the topography within the subset of grid points at which we predict failure to occur during that time step. The details of model implementation for surface processes of hillslope diffusion and river incision are explained in *Shelef and Hilley* [2013].

The stochastic landslides are implemented in the landscape evolution simulation in the following way. For each topographic grid cell, we calculate the probability of failure within a time step by multiplying the failure rate (t^{-1}) with a time interval (i.e., 100 yr) (hereafter, failure probability; 0 for impossible and 1 for certain failure). The failure probability is compared to a value randomly drawn from the uniform distribution in the interval (0, 1). If the calculated failure probability exceeds the randomly drawn value, a landslide is triggered and the elevation is lowered by landslide thicknesses. The landslide thickness is calculated as elevation difference during a slope adjustment between surface slope and failed slope in scenario SD and set to 1 m in scenario SS. We assume that the failed material is transported out of the river network within a single time step and estimate the amount of surface lowering for each time step. For scenario SS, we assume that the soil will be produced or transported within a given time step and be available to fail in the next time step. The assumptions of instantaneous evacuation of failed landslide

Table 2. Summary of Basin Characteristics and Denudation Rates and Response Time Scale

							Scenario SD1				Scenario SS1		
							Denudation Rate				Denudation Rate		
Sample Name	Latitude (°)	Longitude (°)	Drainage Area (km^2)	Long-Term Uplift Rate[a] (mm/yr)	CRN-Derived Denudation Rate[b] (mm/yr)	1σ	Best Fit[c] (mm/yr)	(0–5 kyr)[d] Mean	(0–1000 kyr)[e] Time-Invariant	Time Scale[f] kyr	Best Fit[c] (mm/yr)	(0–5 kyr)[d] Mean	Time Scale[g] kyr
WR1	47.821	−120.422	525.0	0.03	0.24	0.02	0.16	0.19	0.16	-	0.18	0.17	903
WR2	47.737	−120.369	235.8	0.03	0.13	0.01	0.07	0.08	0.08	-	0.08	0.08	463
WR3	47.663	−120.251	1074.1	0.03	0.17	0.01	0.11	0.13	0.12	-	0.12	0.12	683
WR4	47.843	−120.665	445.9	0.03	0.43	0.03	0.21	0.24	0.18	125	0.22	0.21	958
WR5	47.769	−120.802	238.0	0.04	0.28	0.02	0.21	0.27	0.16	140	0.24	0.24	768
WR6	47.688	−120.739	103.3	0.04	0.20	0.01	0.28	0.34	0.24	185	0.27	0.28	858
WR7	47.543	−120.717	500.0	0.06	0.23	0.02	0.27	0.31	0.24	100	0.28	0.28	763
WR8	47.548	−120.611	345.7	0.07	0.08	0.01	0.12	0.15	0.14	-	0.14	0.14	313
WR9	47.803	−121.293	172.6	0.09	0.41	0.03	0.25	0.31	0.17	125	0.29	0.29	363
WR10	47.819	−121.555	377.2	0.11	0.54	0.04	0.51	0.60	0.25	140	0.42	0.41	443
WR11	47.837	−121.659	1384.6	0.14	0.57	0.04	0.41	0.49	0.23	145	0.35	0.35	283
MH17	47.656	−121.293	126.2	0.20	0.46	0.03	0.49	0.61	0.26	180	0.38	0.38	178
MH22	47.714	−121.168	61.0	0.08	0.43	0.03	0.30	0.35	0.14	170	0.31	0.31	473

[a]Basin averaged long-term million-year-time scale uplift rates from A-He ages [*Reiners et al.*, 2002, 2003] (Figure S1 in the supporting information).
[b]CRN-derived denudation rates are measured from cosmogenic ^{10}Be concentration, representing thousand-year-time scale denudation rates [*Moon et al.*, 2011].
[c]Expected denudation rates from Bayesian best fit parameters using the exhaustive search results.
[d]The averages of simulated denudation rates for initial 0 to 5 kyr.
[e]The time-invariant denudation rate defined 5 kyr averaged denudation rate, filtered with a 25 kyr averaging window, shows a variation of less than 1% for 10 time steps (50 kyr).
[f]The decay time scale is determined by the approach of the 5 kyr averaged denudation rate, filtered with a 25 kyr averaging window, to a time-invariant rate. Samples whose time invariant rate lies within 1σ range of initial 0–5 kyr denudation rates are excluded.
[g]The response time scale when the 5 kyr averaged denudation rate lies within 40% of long-term uplift rates.

material and production/transport of soil within the modeled time step may not be plausible in real landscapes. We discuss potential impact of these assumptions on the response time scale in section 4.1. By applying overall elevation changes due to uplift rates (Figure S1 in the supporting information) and surface processes over time, we examine how the topography and denudation rates will evolve as the deglaciated landscape adjusts its form to postglacial surface processes. Additional details of the model (such as spatial and temporal discretization) is elaborated in the supporting information.

3. Results

3.1. Calibration of Model Parameters

The best fit parameters for stochastic landslides and detachment-limited river incision are identified by the minimum of WRSS value in the exhaustive search. The best fit parameters for scenario SD, hereafter referred to SD1, are $K_d = 1.0 \times 10^{-6}\,m^0\,yr^{-1}$, $T = 1.1 \times 10^3\,m^2\,yr^{-1}$, $P_{max} = 4.0 \times 10^{-9}\,m^{-2}\,yr^{-1}$, $FI_{max} = 1$, and $S_0 = 1$ (Table 1). The expected denudation rates from current topography with the best fit parameters vary from 0.07 to 0.51 mm/yr (Table 2), while the CRN-measured denudation varied from 0.08 to 0.57 mm/yr [*Moon et al.*, 2011]. There is a good correlation between the expected and measured erosion rates ($R^2 = 0.669$) (Figure 5). The root-mean-square error between the CRN-derived denudation rates and expected denudation rates from the best fit parameter is ±0.11 mm/yr. This corresponds to 33% of the average of CRN-derived denudation rates of the Cascades. Assuming that our samples are well mixed, the model results from SD1 predict basins in the west have more contributions from landslides (63–79%) than those in the east (11–65%) (Table S1 in the supporting information). The basin with the highest expected denudation rate, WR10 in the west, also had the highest contribution to erosion from landslide processes (79%). In contrast, the basin with the lowest denudation rate, WR2 in the east, has the lowest denudation rates and the highest contribution from river incision (89%).

We estimate the probability distribution of the a posteriori model parameters using χ^2 and Bayes' theorem. With ~7% measurement errors of CRN-derived denudation rates for σ^{meas}, the χ^2_{meas} is 35.87. This high χ^2 results from the small uncertainties for the measured denudation rates. To account σ^{meas} as an overall

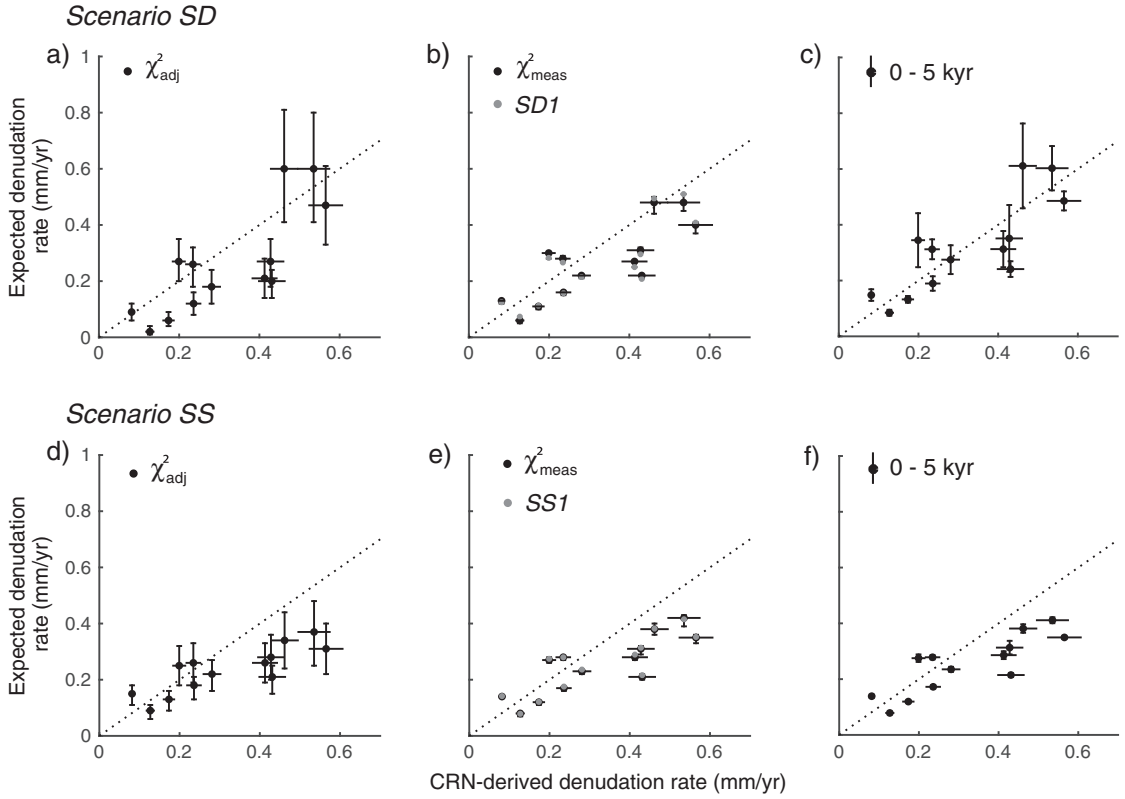

Figure 5. Plots of CRN-derived denudation and the range of the expected denudation rates from scenarios of (a–c) SD and (d–f) SS. Expected denudation rates are from parameter calibrations (Figures 5a, 5b, 5d, and 5e) and model simulation (Figures 5c and 5f). The probability of expected denudation rates with given parameters, $P(x|m)$, is calculated from χ^2_{adj} (Figures 5a and 5d) and χ^2_{meas} (Figures 5b and 5e). The black circles represent the median, and the error bars represent the 1σ range of the probability distribution of a posteriori expected denudation rates. The gray circles indicate the expected denudation rates from current topography and the best fit parameters (SD1 and SS1). Plot of CRN-derived denudation rates with 1σ uncertainties and the range of the simulated denudation rates averaged over first 50 time steps (0–5 kyr) with 1σ range in error bars (Figures 5c and 5f).

model inaccuracy that can be larger than analytical uncertainties, we adjust σ^{meas} to produce $\chi^2 = 1$ with the best fit parameters (χ^2_{adj}). The adjusted σ^{meas} corresponds to ~42% uncertainties in CRN-derived denudation rates. Using χ^2_{adj}, we calculate the a posteriori probability distributions of the model parameters $P(m|x)$ (Figures 3 and 4). The 95% credible interval (CI) of marginal probability distribution is 0.1–$2.0\times10^{-6}\,m^0\,yr^{-1}$ for K_d, 0.4–$2.8\times10^3\,m^2\,yr^{-1}$ for T, 0.2–$25.1\times10^{-8}\,m^{-2}\,yr^{-1}$for P_{max}, 5–29 for FI_{max}, and 0.5–0.9 for S_0. The median and 1σ range of probability of the expected denudation rates based on χ^2_{adj} and χ^2_{meas} are shown in Figure 5 and Table S1 in the supporting information. The χ^2_{adj} produces a larger range of expected denudation rates than χ^2_{meas}.

The marginal and two-dimensional joint probability distribution help to examine the uncertainties within and covariations between model parameters. Because the best fit parameters are determined from the highest probability at five-dimensional joint pdf, the values at the highest probability in marginal or two-dimensional joint pdfs do not necessarily correspond to the location of best fit parameter values (Table 1). The marginal probability distribution of parameters from χ^2_{adj} shows that K_d and P_{max} are well constrained compared to T, FI_{max}, and S_0 (Figure 3). The probability of T, FI_{max}, and S_0 increases with each value (Figures 3b, 3d, and 3e). The joint pdf of K_d and P_{max} shows that a high probability zone has maximum bounds for both values (Figure 4b). The joint pdf of T and P_{max} defines a closed zone of high probability (Figure 4d). The joint pdfs of both P_{max} and FI_{max} and P_{max} and S_0 show that the high-probability zone lies along a positive slope (Figures 4f and 4i). This indicates that covariations between parameters of P_{max} and FI_{max} and P_{max} and S_0 can produce similar model fit. In fact, the second minimum of WRSS in the exhaustive search for scenario SD, hereafter referred to SD2, are $K_d = 1.0\times10^{-6}\,m^0\,yr^{-1}$, $T = 0.9\times10^3\,m^2\,yr^{-1}$, $P_{max} = 25.0\times10^{-9}\,m^{-2}\,yr^{-1}$, $FI_{max} = 12$, and $S_0 = 0.9$ with χ^2_{meas} of 35.93. These

parameters have similar K_d but very different P_{max} and FI_{max}. The parameters of SD2 also produce similar denudation rates, showing a good correlation with CRN-derived denudation rates ($R^2 = 0.666$).

We also optimize five model parameters for scenario SS. The best fit parameters for scenario SS, hereafter referred to SS1, have lower K_d and higher P_{max} values than scenario SD (Table 1 and Figure S3 in the supporting information). SS1 predicts that sediments are mostly derived from landslides (~100%), while few are sourced from river incision. The best fit K_d is $1.0 \times 10^{-9}\,m^0\,yr^{-1}$, and the best fit P_{max} is $2.5 \times 10^{-6}\,m^{-2}\,yr^{-1}$ with FI_{max} of 29. The corresponding failure density at failure condition ($P_{FI=1}$) is $4.4 \times 10^{-8}\,m^{-2}\,yr^{-1}$, which is an order of magnitude higher than SD1. The marginal and joint probability distributions of parameters in scenario SS show similar distributions with those in scenario SD (Figure 3 and Figure S3 in the supporting information). The minimum χ^2_{meas} of this scenario is 39.0, which is higher than those of SD1 (35.9). The expected denudation rates from SS1 also show a good correlation with CRN-derived denudation rates ($R^2 = 0.705$; Figure 5) but underestimate the high denudation rates.

3.2. Simulation of Postglacial Processes and Topographic Evolution

Using the model fit parameters, we simulated the evolution of the topography and denudation rates of the Washington Cascades to estimate the response time scales of deglaciated landscapes. Simulated denudation rates from scenario SD1 averaged over 0 to 5 kyr correspond well with CRN-derived denudation rates and the expected denudation rates from current topography with the best fit parameters (Figures 5b and 5e). The relative standard deviation of simulated denudation rates (1σ/mean) range from 7 to 34% with an average 17% for our studied basin. Three basins (WR6, MH17, and MH22) with small drainage areas have larger mean relative standard deviation (25–34%).

Simulated denudation rates decay as surface processes preferentially modify steep topography. Denudation rates from basins that experienced limited glacial scour during the Last Glacial Maximum (LGM) have less decay throughout model simulation relative to simulated basins with high glacial scouring (e.g., WR2, WR3, and WR8, whose areas of which were less than 75% glaciated [*Moon et al.*, 2011]). We define landscape response time as the time to take for 5 kyr averaged simulated denudation rates to be within ±40% uncertainty of the million-year-time scale uplift rate. We assigned 40% uncertainty considering the overall model inaccuracy σ^{adj} (~42%). MH17 and WR11 have response times of 150 and 210 kyr, respectively. However, denudation rates from the other basins decay to values higher than million-year-time scale uplift rates. After they reach certain rates, they sustain similar values or slightly increase during the simulation time. To obtain the overall, long-term pattern from 5 kyr averaged denudation rates that still show stochastic variations, we filter 5 kyr averaged denudation rates with a 25 kyr averaging window. A time-invariant denudation rate that is defined as 5 kyr averaged denudation rate, filtered with a 25 kyr averaging window, shows a variation of less than 1% for 10 time steps (50 kyr). The time-invariant rates vary from 0.08 to 0.26 mm/yr and are reached around 100–185 kyr. These rates are roughly comparable to million-year-time scale uplift rates (0.03–0.20 mm/yr) but are on average 0.11 (0.05–0.20) mm/yr higher than the uplift rates (Table 2).

To examine the role of the chosen model parameters and assumptions, we also determine the response time scales for other scenarios. We simulate the topographic evolution of the second best fitting parameters for scenario SD (SD2) and the best fitting parameters for scenario SS (SS1). In SD2, the denudation rates slightly increase in the first ~20 kyr, then decay over time. Simulated denudation rates reach time-invariant rates around 150–310 kyr (Figure S5 in the supporting information) and vary from 0.09 to 0.27 mm/yr. Denudation rates of SS1 show different temporal evolution from scenario SD. Denudation rates from individual model time steps show less variation due to landslides with smaller volumes and decay more linearly than those from scenario SD. Over the simulation, denudation rates continuously decline and do not reach time-invariant rates during the simulation. In this scenario, response time scales reach $<$±40% uncertainties of the million-year-time scale uplift rates vary between 180 and 960 kyr. The response time scales in the west are shorter (180–480 kyr), while they tend to be longer for basins in the east (310–960 kyr).

To examine how the spatial distribution of denudation processes changes over time, we show the spatial distribution of time-averaged denudation rates over 40 kyr from 0 to 120 kyr (Figure 7). The simulation based on SD1 illustrates that in the initial 40 kyr, landslides with larger depth occupy the steep regions of this landscape on the sidewalls near the bottom of oversteepened glacial valleys and on high peaks.

As a result, denudation rates are very high for those regions (Figure 7a). Simulation based on SS1 shows that denudation rates are higher in the regions with higher slopes, indicating that those areas fail more frequently during time steps. Since discrete landslides in this scenario erode only 1 m, steep regions are maintained for longer than in scenarios SD1 and still produce high denudation rates in the later time periods (80–120 kyr) (Figure 7f). Overall, more landslides occur in western basins due to the higher precipitation rates and steeper slopes inherited from previous glaciations (Figure S6 in the supporting information).

4. Discussion

4.1. Impact of Landslide Model Assumptions

Our landslide model relies on several assumptions that limit the applicability of this approach. First, we use a slope stability model designed for shallow landslides to assess the slope stability for landslides whose depths extend to bedrock (scenario SD). *Montgomery and Dietrich* [1994] originally proposed their physically based slope stability model to assess the stability of shallow landslides whose spatial extent is in the order of tens of meters and whose failure plane is located on the bedrock-soil interface (~1 m). The landslide thickness of shallow landslides in *Montgomery and Dietrich* [1994] are similar to 1 m landslide thickness in scenario SS. However, our scenario SD typically has landslide depths deeper than the bedrock-soil interface. The potential depth of landslide failure surfaces is ~18 m on average and up to 417 m based on best fit S_0 and T in SD1.

The coupled slope stability and steady state hydrologic model has been used to assess the bedrock landslide based on the degree of water saturation of a rock mass above a failure plane by *Günther et al*. [2004]. They assumed that the bedrock above the failure plane was a continuous hydrologic unit, such that groundwater flow is determined by the orientations of all surrounding transmissive layers. They used the topographic gradient to assess the extent of shallow groundwater saturation during rainfall events. Their assessment of groundwater saturation was supported by measurements of runoff and groundwater pressure head, as well as the properties of hillslopes in the study area with fractures extending to depths of ~20 m. Previous studies in the Cascades in southern Washington have also shown that the hydraulic gradient of groundwater is similar to that of the topographic gradient and that fractures in bedrock are the primary source of porosity [*Vaccaro et al*., 2009; *Gendaszek et al*., 2014]. Additionally, these studies have reported rapid groundwater fluctuations in the fractured crystalline rocks during rainfall events, suggesting that near-surface transport of groundwater responds quickly to short-term rainfall events. In this study, we therefore adopt the approach of *Günther et al*. [2004] and use topographic wetness as a simple first-order approximation of the degree of saturation of bedrock layers as well. In this regard, we use the GTL form for both scenarios SD and SS, optimize the model parameters for each scenario, and examine the potential ranges of the response time.

Second, we assume that the landslide areal size is fixed to the size of a grid cell. Our approach considers topographic and climatic controls that determine individual landslide occurrences. However, because the simulated landslide area is fixed, it cannot simulate commonly observed landslide size-frequency distributions [*Hovius et al*., 1997; *Stark and Hovius*, 2001]. In the Pacific Northwest, *Montgomery et al*. [1998] compiled an inventory of 3224 landslides and computed their size distribution. Most landslides (~90%) have areas less than 10,000 m^2, with a mean size of ~8000 m^2, and very few landslides have areas larger than 20,000 m^2. These data suggest that the fraction of landslides larger than our cell size (10,000 m^2) is ~10%, which should be considered as an upper bound as very small landslides are often unmapped. Thus, rather than implementing a multiple-cell failure model, we focus on constraining the average failure density (landslides $m^{-2} yr^{-1}$) within our grid cell size based on measured denudation rates and explore the ranges of potential landscape response time scale based on the two landslide thickness scenarios. However, we cannot rule out the possibility that a multiple-cell failure model, in which increased landslide areas result in greater landslide thicknesses, may increase denudation rates and shorten estimates of the response times. The artifacts resulting from a grid-cell discrete landslide are evident in SD2. In SD2, we observe that the number of points that are affected by landslides slightly increases, and high denudation rates are sustained for the initial ~20 kyr (Figure S5 in the supporting information). This is related to the implementation of a grid-cell-wise landslide and its upslope propagation though time. The removal of

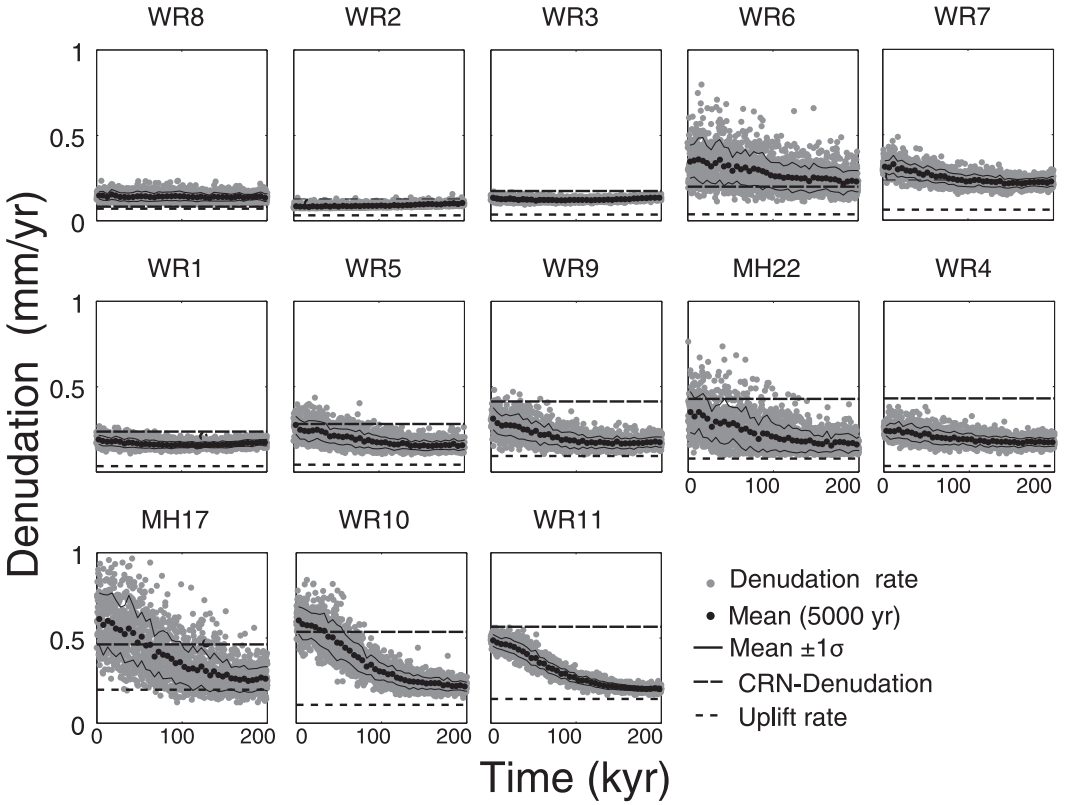

Figure 6. The evolution of denudation rates from postglacial processes based on the scenario SD1. Basins are shown in ascending order of the CRN-derived denudation rates. Each panel shows the time scale from 0 (present) to 200 kyr. The gray points show the denudation rates from all time steps, and the black circles represent the averages using a 5 kyr moving window. The 1σ range within the 5 kyr averaging window is shown as solid lines. We show the results of simulated denudation rates on the same axis scale from 0 to 1 mm/ yr. Basins WR8, WR2, and WR3 were less than 75% glaciated during the LGM resulting in initial postglacial denudation rates similar to uplift rates.

material via the initial failure of a grid cell will lower its elevation and increase the slope of the upstream neighbors during a time step. This will in turn increase the probability of failure for these upstream cells in future time steps and produce the initial increase of denudation rates. This may contribute to the longer decaying time observed in SD2 as compared to SD1 (Figure 6 and Figure S5 in the supporting information).

Third, we assume simple forms of GTLs and use a limited number of surface processes in our analysis. The simplified formulations and limited use of GTLs are intended to minimize the number of parameters in GTLs to improve the parameter search using statistical methods. Since we have limited information (e.g., CRN-derived denudation rates, A-He ages, topography, and precipitation), we focus on optimizing a few variables critical for postglacial surface processes like landslides (e.g., T/q and P_{max}), which are suggested to be a dominant sediment source in deglaciated landscapes [*Dadson and Church*, 2005; *Doten et al*., 2006; *Norton et al*., 2010b; *Moon et al*., 2011].

We assume spatially uniform hydrologic properties of rock (uniform T). Transmissivity T is expected to vary with lithology, soil depth, vegetation, and scale. Since mostly granitic and metamorphic rocks floor our studied basins, the assumption of uniform lithology may be valid. Ignoring surface soil, uniform lithologies in our area may produce relatively uniform mean bedrock transmissivity at depth. However, it may be inappropriate in other areas with different rock types (i.e., sedimentary rocks) [*Hunting et al*., 1961]. While variations in T over short length scales may also arise due to changes in fracture networks and soil depth, the dearth of field data available to constrain spatial variations in T complicate the definition of a spatially variable distribution of T in our model. As such, we assign a uniform value for T but acknowledge that this parameter could be varied in space and time as more information relating its variation to other modeled properties are formulated.

We use the spatial distribution of mean annual precipitation (MAP) averaged between 1971 and 2000 [*PRISM*, 2006] to represent the spatial distribution of steady state precipitation (q) for a storm event in the model. Previous studies have used precipitation as a threshold control that can initiate landslides [*Montgomery and Dietrich*, 1994]. We assume that higher precipitation will increase pore water pressure on the failure surface and thus increase probability of failure and landslide frequency [*Reid*, 1998; *Turner et al*., 2010]. Previous studies in this region showed that the maximum 24 h rainfall intensity shows a similar spatial distribution with MAP due to a significant orographic effect on precipitation [*Wallis et al*., 2007]. This suggests that the relative spatial distribution of MAP may mimic the overall distribution of rainfall intensity of individual storm events that likely generate landslides. Thus, we use the spatial distribution of MAP to represent rainfall intensity (q). We also assume that this spatial distribution of MAP will be consistent over the modeled time scale (~1 Myr). Since paleoclimate studies show that the relative distribution of precipitation has been consistent since 8–15 Ma [*Takeuchi and Larson*, 2005], this assumption is somewhat defensible.

We did not account for the spatial variation of precipitation for river incision processes like most of other landscape modeling studies on postglacial fluvial processes [*Braun et al*., 1999; *Dadson and Church*, 2005; *Norton et al*., 2010a]. Although erosional efficiency, K_d, for river incision should be a function of precipitation based on the stream power law, many studies have found it difficult to resolve the impact of this effect on incision dynamics [*Stock and Montgomery*, 1999; *Snyder et al*., 2000]. In contrast, the climatic controls on landslide processes are commonly observed [*Reid*, 1998; *Turner et al*., 2010]. This may be due to K_d being also affected by other factors such as critical shear stress, lithology, erosional processes, and sediment supply. Since we lack information to constrain those parameters of river incision, we used a simple GTL and spatially uniform K_d.

An important surface process that we did not include in our landscape model is alluvial transport. Instead, we assume that sediment generated by mass failure will be transported through the model domain in less than a model time step (100 year). Because the Cascades are characterized by a relatively humid climate (500–5000 mm/yr) and the studied basins have large drainage areas with high-order streams, we assume that those rivers have a high transport capacity capable of transporting the sediments [*Tunnicliffe and Church*, 2011]. In reality, the sediments from large landslides can reside in the flat glacial valley bottom for substantial periods of time and those impoundments may decrease both incision and transport efficiency of the channels. Indeed, some of the Quaternary glacial deposits are still present in deglaciated valleys [*Hunting et al*., 1961], and large boulders are present in channels along glacial valleys. If sediment cover acts to retard channel incision, our response time scale should likewise be longer. In addition, we did not include nonlinear, diffusive hillslope transport processes [*Roering et al*., 1999]. If we include nonlinear diffusive transport process, our landslide sediment flux will be compensated and optimized to lower failure density. Since our landslide GTL assumes instantaneous transport, its compensation with nonlinear hillslope transport will lengthen the response time scale.

We also did not take into account soil production processes. In SS1, when a landslide occurs, we assume that 1 m of soil will be transported and reproduced during our modeled time step (100 year) and therefore be available to fail in the next time step. This corresponds to a grid-cell averaged soil production rate of ~10 mm/yr and basin-averaged soil production rates ranging from 0.08 to 0.42 mm/yr. The maximum soil production in the Oregon Coast Ranges was measured as 0.3 mm/yr at zero soil depth [*Heimsath et al*., 2001], which is lower than our assumed rates of 10 mm/yr. If we assume that the amount of failed material is solely controlled by soil production rate, this will result in lower landslide rates due to the reduced amount of failed material. This will ultimately have the effect of increasing the response time scales.

Lastly, we assume that our ^{10}Be-measured denudation rates are representative of basin-averaged denudation. The bedrock landslide sediments from deeper depths tend to have low ^{10}Be concentrations, so the input of these sediments can bias our measured denudation rates and model parameters to higher values. Previous studies showed CRN concentrations produce a reliable basin-average denudation rate in regions dominated by bedrock landslides when sampled from a larger catchment area ($>100\,km^2$) [*Niemi et al*., 2005; *Yanites et al*., 2009]. Considering that most of our sampled basin has drainage areas larger than $100\,km^2$, except for MH22 ($60\,km^2$), it is appropriate to use denudation rates to calibrate our model. In

addition, even if the input of bedrock landslides produced higher calibrated model parameters, this would lead to a rapid landscape response. This suggests that we should consider our response time scale estimates as a minimum. While we make a number of assumptions, many of those assumptions likely produce response time scales faster than what might be expected in reality. As a result, our reported response time scales are likely minimum estimates of response time scale.

4.2. The Rates and Controls of Postglacial Surface Processes

We calibrate the model parameters of river incision, K_d, and stochastic landslides, T, P_{max}, FI_{max}, and S_0, based on CRN-measured denudation rates. The magnitude and distribution of expected denudation rates from the model are highly dependent on the model parameter choices. The marginal probability distribution of the a posteriori parameters shows that the range of K_d and P_{max} with high probability is better defined than those of T, FI_{max}, and S_0. This suggests that these parameters factor heavily into the correspondence between expected and measured denudation rates. The upper bounds of the probability of K_d and P_{max} are constrained better than the lower bounds (Figure 4b). This is expected because higher K_d and P_{max} can produce rates much higher than CRN-derived denudation rates, which will result in high χ^2 values and extremely low probability.

Optimized values of parameters can vary by an order of magnitude for different modeled scenarios. The optimized K_d in SD1 ($1.0\times10^{-6}\,m^0\,yr^{-1}$) is 3 orders of magnitude higher than that in SS1 ($1.0\times10^{-9}\,m^0\,yr^{-1}$). Considering the reported values for K_d of similar rock types in Australia (10^{-7} to $10^{-6}\,m^{0.2}yr^{-1}$) [*Stock and Montgomery*, 1999], the K_d in SD1 is more plausible. The extremely low K_d and limited river incision may not be likely in this study region but are affected by optimization with our landslide rule with constant depth. This suggests that the spatial variation of denudation rates is explained better with a landslide rule in which landslide depth scales with climate or topography to some degree. In addition, SD1 produced a failure density at $FI=1$ ($P_{FI=1}$) as $0.4\times10^{-8}\,m^{-2}\,yr^{-1}$ with an average potential failed depth of ~18 m, while SS1 produced the $P_{FI=1}$ as $4.4\times10^{-8}\,m^{-2}\,yr^{-1}$. The lower $P_{FI=1}$ in SD1 than SS1 suggests that comparable denudation rates can be achieved with infrequent, larger landslides or more frequent, smaller landslides.

The failure density from SS1 in the Cascades is higher than the range of the long-term failure density of shallow landslides on the Oregon Coast ranges, which is estimated as $1–3\times10^{-8}\,m^{-2}\,yr^{-1}$ with the same soil depth of 1 m [*Montgomery et al.*, 2000]. The calculation is based on 80–100 hollows/km^2 with 3–8 kyr recurrence interval measured from ^{14}C dating from basal colluviums. Our model scenario SS1 predicts more frequent shallow landslides in the Cascades than those in the Oregon Coast ranges. This increased failure density in deglaciated landscapes is likely due to oversteepened slopes considering the similar climatic settings [*PRISM*, 2006].

The joint a posteriori pdfs show that there are covariations between P_{max} and FI_{max} and P_{max} and S_0. This covariation may emerge due to the prescribed, a linear relationship between FI and P_{max} with a linear coefficient of $(P_{max}\text{-}P_{min})/(FI_{max}\text{-}FI_{min})$ (Figure 2). The $(P_{max}\text{-}P_{min})/(FI_{max}\text{-}FI_{min})$ is the same with the twice of $P_{FI=1}$ (Figure 2). Considering the slope distribution of our studied basin (interquartile range of 0.29–0.63), 75% of our topographic grid cells will have $FI<1.2$. The high probability lies where the combination of landslide parameters, P_{max}, S_0, and FI_{max}, can constrain the failure density of most topographic grid cells (e.g., $P_{FI=1}$). This argument is supported by the range of 95% CI of $P_{FI=1}$, which is 1 order of magnitude narrower than those of P_{max} (Table 1). In addition, this covariation likely produces a linear increase in marginal probability of FI_{max} and S_0 in Figure 3 because higher values of FI_{max} and S_0 produce similar model fits with larger range of P_{max} (see Figures 4f and 4i).

The broader pdf of transmissivity T implies that the magnitudes of denudation rates are less sensitive to T than P_{max}. Variations in T will change wetness and therefore $k(W)$, but the 2 order of magnitude variation of T will only result in a range of (0, 1) in wetness and (1, 2) in $k(W)$. Although transmissivity T appears less important in determining the magnitude of basin-averaged denudation rates, it does impact the spatial distribution of denudation rates. The a posteriori T distribution has a narrower range of high probability when using smaller, measured uncertainties, σ^{meas}, than when using larger, adjusted uncertainties, σ^{adj} (gray lines in Figure 3b). The best fit T values from both SD1 and SS1 are optimized to maximize the spatial

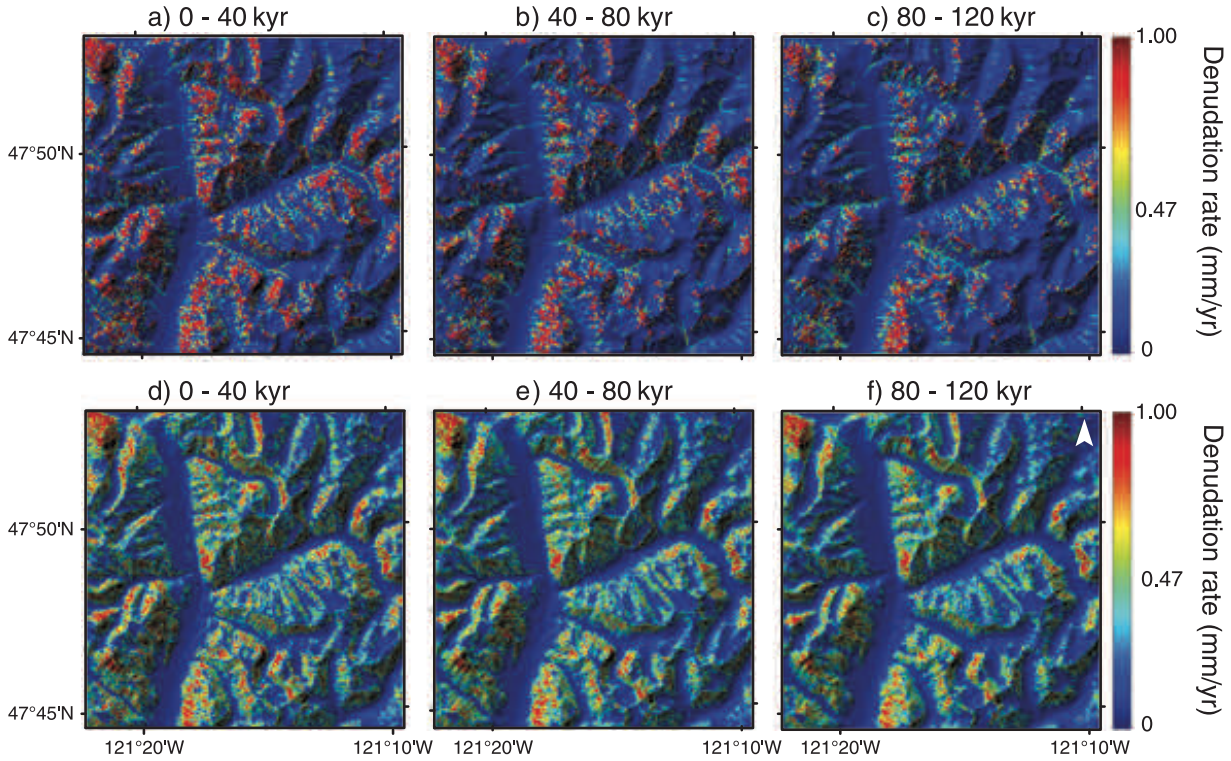

Figure 7. The spatial distributions of time averaged denudation rates of the WR9 basin over 0–40 kyr, 40–80 kyr, and 80–120 kyr from simulation results from scenarios of (a–c) SD1 and (d–f) SS1. Warm colors, drawn on a shaded relief map at the initial time (0, 40, and 80 kyr), represent areas with higher denudation rates. The full extent of model domain is shown in Figure S6 in the supporting information.

variation of $k(W)$. The best fit T value is ~3 m^2/d (~1100 m^2/yr) in SD1, which is more than an order of magnitude lower than ~65 m^2/d of *Montgomery and Dietrich* [1994]. This is largely because our measure of q (MAP) is lower than that produced by rainfall intensity from storms. For example, the rainfall intensity of 24 h maximum rainfall with 10 year return periods varies from 85 to 173 mm in our basins, which are approximately 20–30 times higher than MAP [*Wallis et al.*, 2007]. Based on the best fit T value from SD1, the basin-averaged T/q varies from 350 (WR10) to 1170 m (WR2). *Montgomery and Dietrich* [1994] used values of the hydrologic parameter T/q of ~ 350 m as a lower limit representing a saturated condition. This value is similar to our basin-averaged T/q in the west that is largely affected by increased pore pressure due to higher precipitation than eastern counterpart. The similar range of the calibrated hydrologic parameter T/q between our study and *Montgomery and Dietrich* [1994] suggests that the optimized T/q from statistical model provides a good estimate for the spatial distribution of the hydrologic parameter in the study area.

4.3. Topographic and Erosional Evolution of Deglaciated Landscapes

Using the calibrated parameters for modeling river incision and stochastic landslides, we examine the evolution of topography and denudation rates in the Washington Cascades as the landscape adjusts its form to postglacial processes. Landslide processes preferentially denude the steep regions of deglaciated landscapes, including oversteepened valley walls near the bottom of glacial valleys and the peaks above the glacial equilibrium line during LGM (Figure 7 and Figure S6 in the supporting information). The landslide inventory in our study area also shows that mapped landslides are near those steep regions [*Boyd and Vaugeois*, 2003] (Figure 1). This is consistent with other studies in deglaciated landscapes, which showed that debris flows and landslides occurs in the glacially-steepened valleys [*Norton et al.*, 2010b].

The scenario-based simulations allow us to examine the temporal evolution of denudation rates and the potential ranges of response time scales of denudation rates. In SD, due to the prevalence of landslides with large volumes, denudation rates have larger variations. The instantaneous removal of those landslide

materials leads to a rapid exponential decay of denudation rates. In this scenario, simulated denudation rates asymptotically decay toward time-invariant rates that are comparable to, but higher than million-year-time scale uplift rates. The higher time-invariant rates may be due to the increased river incision rates resulting from reorganized stream networks and channelized drainage basins in the deglaciated landscapes (Figure 7). Basins that require large reorganizations of some of the watershed drainage areas produce large differences between the time-invariant rates and uplift rates (e.g., WR6 and WR7; 0.20 and 0.18 mm/yr, respectively). Previous work suggests that the reorganization of drainage network for fluvial system may take approximately 1 to 3 times the duration that erode an interval equivalent to the relief of the mountain belt (e.g., 5–15 Myr in this study area) [*Howard*, 1994; *Whipple*, 2001]. This is much longer than our modeled timespan (1 Myr), and the time scales for the initial pulse of postglacial denudation rates from landslides to decay to time-invariant rates (100–960 kyr in SD1 and SS1). Another possibility is that our landslide rule creates steep landscapes with threshold slopes after slope failure and that these steep landscapes produce higher denudation rates from hillslope transport and river incision. In reality, local deposition of debris on proximal slopes and valley floors can reduce the slopes after each failure, which can produce lower denudation rates than our model predicts. The landscape model based on scenarios SD and SS provides an opportunity to examine the decay of landslide frequency and overall denudation rates from landslides following deglaciation. Both scenarios predict that denudation rates will decay over time scale over time scales of 100–960 kyr, and the basins in the western Cascades influenced strongly by deglaciation will decay over 100–480 kyr.

Our estimated response time scale is based on several assumptions and accordingly has uncertainty. As discussed above, the inclusion of soil production and sediment transport in channels and on hillslopes would increase the time required to reach time-invariant rates [*Baldwin et al*., 2003; *Gasparini et al*., 2007; *Egholm et al*., 2013]. Therefore, our response time scale should be viewed as a minimum. The estimated minimum response time scale is still significantly longer than the times since the last deglaciation (11–17 kyr) [*Porter*, 1976] and the time scale of CRN-derived denudation rate measurements (1.1–7.4 kyr). The CRN-derived denudation rates and simulated denudation rates for 0–5 kyr show comparable values considering the uncertainties in simulation (1σ, 17%) (Figure 5), which supports our assumption that CRN-derived denudation rates can be used to calibrate the model parameters of surface processes acting on the current topography. The longer response time of denudation rates is also consistent with a simple visual assessment of current topography that still shows features from previous glaciations with 34% of the area occupied by slopes exceeding 0.5, a commonly observed slope threshold. In addition, the response time scale is longer than the 25 kyr that is expected from the landslide failure density of $0.4 \times 10^{-8}\,\mathrm{m}^{-2}\,\mathrm{yr}^{-1}$ with $\mathrm{FI} > 1$. This indicates that postglacial processes may not consume the steep regions at once and create additional area to fail or continuously denude as the landscape changes over time. Some areas in Figure 7 sustain high denudation rates over time.

The minimum response time scale of the Cascades is shorter than or comparable to the 500 kyr or longer response time scale of the deglaciated landscapes in the northwest Himalaya [*Hobley et al*., 2010]. We attribute that the potential shorter response time scale is due to our inclusion of stochastic landslides and the increase in precipitation received by the Cascades (MAP of 2 m/yr versus 0.1 m /yr in the Tibetan Himalaya). However, our time scale is much longer than the response time scale of 5–10 kyr expected from modeling an idealized glacial valley [*Dadson and Church*, 2005]. The rapid response time of idealized glacial valley in the *Dadson and Church* [2005] is due to the use of high landslide denudation rates in the model (~2.8 mm/yr versus ~0.3 mm/yr in this study) and smaller basin areas (2 km^2 versus 1000 km^2 in this study).

The response time scale of denudation rates from all model scenarios is on the order of or longer than the dominant 100 kyr glacial and interglacial intervals in the Cascades during the Quaternary [*Hays et al*., 1976]. This suggests that the Cascades has not likely reached a steady state condition with postglacial surface processes during interglacial periods in the Quaternary. This may suggest that frequent changes in climates and surface processes regimes such as deglaciation events may increase the chemical and sediment fluxes during interglacial periods in the Quaternary and leave a significant and prolonged impact on denudation and topography. However, to understand the overall landscape evolution of the Cascades during the entire Quaternary, future studies are needed that implement successive glacial and interglacial processes and glacial-isostatic rebound in numerical models [*Braun et al*., 1999].

5. Conclusion

In this study, we model postglacial surface processes in the Washington Cascades using a geomorphic-transport-law-based numerical model that includes river incision, hillslope diffusion, and stochastic landslide processes. We present a GTL for stochastic landslides using the spatial distribution of slope instability and a modeled relationship between slope instability and failure probability. Model parameters of river incision and stochastic landslides are calibrated based on CRN-derived denudation rates using an exhaustive search method. The uncertainties within model parameters and their covariations are assessed using a Bayesian probability. The best fit model parameters are consistent with previous studies in landscapes with similar rock types and climatic conditions. The enhanced postglacial denudation rates in the western Cascades can be explained by modeling of stochastic landslide processes. Specifically, the magnitude of denudation rates is mainly determined by failure density and landslide frequency, while the spatial variation in precipitation sets the distribution of denudation rates.

Using the best fit parameters and current topography as an initial condition, we simulate the evolution of topography and denudation rates in response to the deglaciation event that perturbs the landscape by changing the dominant geomorphic process regime. We use a landscape evolution model with stochastic landslide rules and explore scenarios with different landslide depth configurations. In both scenarios, landslides denude the steep sidewalls of glacial valley and steep peaks preferentially. As the simulation progresses, landslides consume the areas with steep slopes in the deglaciated topography. Overall, the topography and denudation rates decay over time. The expected ranges of decay time scale in basins must exceed 100–960 kyr in the deglaciated Cascades. The time scales of landscape response after deglaciation in these scenarios are still longer than the time scale of major glacial and interglacial cycles (~100 kyr) [*Hays et al*., 1976]. As such, successive glaciations during the Quaternary in the Cascades may produce high denudation rates and leave strong topographic imprints that sustain during glacial cycles.

Acknowledgments

S.M. acknowledges the support of the Stanford Graduate Fellowship and Stanford Center for Computational Earth and Environmental Science facility, and G.E.H. acknowledges the support of the National Science Foundation grant EAR-TECT-240 105581. We would like to thank A. Densmore, J. Pelletier, D. Hobley, S.G. Mitchell, and one anonymous reviewer for their constructive comments. We also would like to thank S. Johnstone, T. Perron, K. Huppert, P. Richardson, and D. Bellugi for their valuable discussions. All data used in this study have been previously published, please see citations in the text.

References

Baldwin, J. A., K. X. Whipple, and G. E. Tucker (2003), Implications of the shear stress river incision model for the timescale of postorogenic decay of topography, *J. Geophys. Res.*, *108*(B3), 2158, doi:10.1029/2001JB000550.

Bayes, R. T. (1763), An essay towards solving a problem in the doctrine of chances, *Philos. Trans.*, *53*, 370–418.

Booth, A. M., J. J. Roering, and A. W. Rempel (2013), Topographic signatures and a general transport law for deep-seated landslides in a landscape evolution model, *J. Geophys. Res. Earth Surf.*, *118*, 603–624, doi:10.1002/jgrf.20051.

Boyd, T. G., and L. M. Vaugeois (2003), On the development of a statewide landslide inventory, *Geol. Soc. Am. Abstr. Programs*, *35*(6), 18.

Braun, J., D. Zwartz, and J. H. Tomkin (1999), A new surface-processes model combining glacial and fluvial erosion, *Ann. Glaciol.*, *28*(1), 282–290.

Culling, W. E. H. (1960), Analytical theory of erosion, *J. Geol.*, *68*(3), 336–344.

Culling, W. E. H. (1963), Soil creep and the development of hillside slopes, *J. Geol.*, *71*(2), 127–161.

Culling, W. E. H. (1965), Theory of erosion on soil-covered slopes, *J. Geol.*, *73*(2), 230–254.

Dadson, S. J., and M. Church (2005), Postglacial topographic evolution of glaciated valleys: A stochastic landscape evolution model, *Earth Surf. Processes Landforms*, *30*(11), 1387–1403.

Davis, W. M. (1899), The geographical cycle, *Geogr. J.*, *14*(5), 481–504.

Densmore, A. L., M. A. Ellis, and R. S. Anderson (1998), Landsliding and the evolution of normal-fault-bounded mountains, *J. Geophys. Res.*, *103*(B7), 15,203–15,219, doi:10.1029/98JB00510.

Dietrich, W. E., D. G. Bellugi, L. S. Sklar, J. D. Stock, A. M. Heimsath, and J. J. Roering (2003), Geomorphic transport laws for predicting landscape form and dynamics, *Geophys. Monogr. AGU*, *135*, 103–132, doi:10.1029/135GM09.

Doten, C. O., L. C. Bowling, J. S. Lanini, E. P. Maurer, and D. P. Lettenmaier (2006), A spatially distributed model for the dynamic prediction of sediment erosion and transport in mountainous forested watersheds, *Water Resour. Res.*, *42*, W04417, doi:10.1029/2004WR003829.

Egholm, D. L., M. F. Knudsen, and M. Sandiford (2013), Lifespan of mountain ranges scaled by feedbacks between landsliding and erosion by rivers, *Nature*, *498*(7455), 475–478.

Gasparini, N. M., K. X. Whipple, and R. L. Bras (2007), Predictions of steady state and transient landscape morphology using sediment-flux-dependent river incision models, *J. Geophys. Res.*, *112*, F03S09, doi:10.1029/2006JF000567.

Gendaszek, A. S., D. M. Ely, S. R. Hinkle, S. C. Kahle, and W. B. Welch (2014), Hydrogeologic framework and groundwater/surface-water interactions of the Upper Yakima River Basin, Kittitas County, Central Washington USGS Scientific Investigations Report 2014–5119.

Griffiths, V. D., and A. G. Fenton (2004), *Probabilistic Slope Stability Analysis by Finite Elements*, pp. 12, Am. Soc. of Civil Engineers, Reston, Va., ETATS-UNIS.

Günther, A., A. Carstensen, and W. Pohl (2004), Automated sliding susceptibility mapping of rock slopes, *Nat. Hazards Earth Syst. Sci.*, *4*(1), 95–102, doi:10.5194/nhess-4-95-2004.

Hack, J. T. (1960), Interpretation of erosional topography in humid temperate regions, *Am. J. Sci.*, *258-A*, 80–97.

Hasbargen, L. E., and C. Paola (2000), Landscape instability in an experimental drainage basin, *Geology*, *28*(12), 1067–1070, doi:10.1130/0091-7613(2000)28<1067:liiaed>2.0.co;2.

Hays, J. D., J. Imbrie, and N. J. Shackleton (1976), Variations in the Earth's orbit: Pacemaker of the Ice Ages, *Science*, *194*(4270), 1121–1132, doi:10.1126/science.194.4270.1121.

Heimsath, A. M., W. E. Dietrich, K. Nishiizumi, and R. C. Finkel (2001), Stochastic processes of soil production and transport: erosion rates, topographic variation and cosmogenic nuclides in the Oregon Coast Range, *Earth Surf. Processes Landforms*, *26*(5), 531–552, doi:10.1002/esp.209.

Hergarten, S., and H. J. Neugebauer (1998), Self-organized criticality in a landslide model, *Geophys. Res. Lett.*, *25*(6), 801–804, doi:10.1029/98GL50419.
Herman, F., and J. Braun (2008), Evolution of the glacial landscape of the Southern Alps of New Zealand: Insights from a glacial erosion model, *J. Geophys. Res.*, *113*, F02009, doi:10.1029/2007JF000807.
Hilley, G. E., and J. J. Young (2008a), Deducing paleoearthquake timing and recurrence from paleoseismic data, Part I: Evaluation of new Bayesian Markov-Chain Monte Carlo simulation methods applied to excavations with continuous peat growth, *Bull. Seismol. Soc. Am.*, *98*(1), 383–406, doi:10.1785/0120020077.
Hilley, G. E., and J. J. Young (2008b), Deducing paleoearthquake timing and recurrence from paleoseismic data, Part II: Analysis of paleoseismic excavation data and earthquake behavior along the central and southern San Andreas Fault, *Bull. Seismol. Soc. Am.*, *98*(1), 407–439, doi:10.1785/0120070012.
Hilley, G. E., I. Mynatt, and D. D. Pollard (2010), Structural geometry of Raplee Ridge monocline and thrust fault imaged using inverse boundary element modeling and ALSM data, *J. Struct. Geol.*, *32*(1), 45–58.
Hobley, D. E. J., H. D. Sinclair, and P. A. Cowie (2010), Processes, rates, and time scales of fluvial response in an ancient postglacial landscape of the northwest Indian Himalaya, *Geol. Soc. Am. Bull.*, *122*(9–10), 1569–1584, doi:10.1130/b30048.1.
Hobley, D. E. J., H. D. Sinclair, S. M. Mudd, and P. A. Cowie (2011), Field calibration of sediment flux dependent river incision, *J. Geophys. Res.*, *116*, F04017, doi:10.1029/2010JF001935.
Hovius, N., C. P. Stark, and P. A. Allen (1997), Sediment flux from a mountain belt derived by landslide mapping, *Geology*, *25*(3), 231–234, doi:10.1130/0091-7613(1997)025<0231:sffamb>2.3.co;2.
Howard, A. (1994), A detachment-limited model of drainage basin evolution, *Water Resour. Res.*, *30*(7), 2261–2286, doi:10.1029/94WR00757.
Howard, A., and G. Kerby (1983), Channel changes in badlands, *Geol. Soc. Am. Bull.*, *94*(6), 739–752.
Hren, M. T., G. E. Hilley, and C. P. Chamberlain (2007), The relationship between tectonic uplift and chemical weathering rates in the Washington Cascades: Field measurements and model predictions, *Am. J. Sci.*, *307*(9), 1041–1063, doi:10.2475/09.2007.01.
Hunting, M. T., W. A. G. Bennett, V. E. Livingston Jr., and W. S. Moen (1961), *Geologic Map of Washington*, 2 plates, Wash. State Div. of Mines and Geol., Olympia, Scale 1:500,000.
Iverson, R. M. (2000), Landslide triggering by rain infiltration, *Water Resour. Res.*, *36*(7), 1897–1910, doi:10.1029/2000WR900090.
Kober, F., K. Hippe, B. Salcher, S. Ivy-Ochs, P. W. Kubik, L. Wacker, and N. Hählen (2012), Debris-flow-dependent variation of cosmogenically derived catchment-wide denudation rates, *Geology*, *40*(10), 935–938, doi:10.1130/g33406.1.
Mitchell, S. G., and D. R. Montgomery (2006), Influence of a glacial buzzsaw on the height and morphology of the Cascade Range in central Washington State, USA, *Quat. Res.*, *65*(1), 96–107, doi:10.1016/j.yqres.2005.08.018.
Montgomery, D. R., and W. E. Dietrich (1994), A physically based model for the topographic control on shallow landsliding, *Water Resour. Res.*, *30*(4), 1153–1171, doi:10.1029/93WR02979.
Montgomery, D. R., K. Sullivan, and H. M. Greenberg (1998), Regional test of a model for shallow landsliding, *Hydrol. Processes*, *12*(6), 943–955, doi:10.1002/(SICI)1099-1085(199805)12:6<943::AID-HYP664>3.0.CO;2-Z.
Montgomery, D. R., K. M. Schmidt, H. M. Greenberg, and W. E. Dietrich (2000), Forest clearing and regional landsliding, *Geology*, *28*(4), 311–314, doi:10.1130/0091-7613(2000)28<311:fcarl>2.0.co;2.
Moon, S., C. Page Chamberlain, K. Blisniuk, N. Levine, D. H. Rood, and G. E. Hilley (2011), Climatic control of denudation in the deglaciated landscape of the Washington Cascades, *Nat. Geosci.*, *4*(7), 469–473, doi:10.1038/ngeo1159.
Niemi, N. A., M. Oskin, D. W. Burbank, A. M. Heimsath, and E. J. Gabet (2005), Effects of bedrock landslides on cosmogenically determined erosion rates, *Earth Planet. Sci. Lett.*, *237*(3–4), 480–498.
Norton, K. P., L. M. Abbühl, and F. Schlunegger (2010a), Glacial conditioning as an erosional driving force in the Central Alps, *Geology*, *38*(7), 655–658, doi:10.1130/g31102.1.
Norton, K. P., F. von Blanckenburg, and P. W. Kubik (2010b), Cosmogenic nuclide-derived rates of diffusive and episodic erosion in the glacially sculpted upper Rhone Valley, Swiss Alps, *Earth Surf. Processes Landforms*, *35*(6), 651–662.
O'Callaghan, J. F., and D. M. Mark (1984), The extraction of drainage networks from digital elevation data, *Comput. Vision Graphics Image Process.*, *28*(3), 323–344, doi:10.1016/S0734-189X(84)80011-0.
Pelletier, J. D. (2004), Persistent drainage migration in a numerical landscape evolution model, *Geophys. Res. Lett.*, *31*, L20501, doi:10.1029/2004GL020802.
Pelletier, J. D. (2010), Minimizing the grid-resolution dependence of flow-routing algorithms for geomorphic applications, *Geomorphology*, *122*(1–2), 91–98, doi:10.1016/j.geomorph.2010.06.001.
Pelletier, J. D., et al. (2011), Calibration and testing of upland hillslope evolution models in a dated landscape: Banco Bonito, New Mexico, *J. Geophys. Res.*, *116*, F04004, doi:10.1029/2011JF001976.
Perron, J. T., J. W. Kirchner, and W. E. Dietrich (2009), Formation of evenly spaced ridges and valleys, *Nature*, *460*(7254), 502–505.
Porter, S. C. (1976), Pleistocene glaciation in the southern part of the North Cascade Range, Washington, *Geol. Soc. Am. Bull.*, *87*(1), 61–75.
PRISM (2006), *United States Average Monthly or Annual Precipitation, 1971–2000*, The PRISM Group at Oregon State Univ., Corvallis, Oreg.
Reid, L. M. (1998), Calculation of average landslide frequency using climatic records, *Water Resour. Res.*, *34*(4), 869–877, doi:10.1029/97WR02682.
Reiners, P. W., T. A. Ehlers, J. I. Garver, S. G. Mitchell, D. R. Montgomery, J. A. Vance, and S. Nicolescu (2002), Late Miocene exhumation and uplift of the Washington Cascade Range, *Geology*, *30*(9), 767–770.
Reiners, P. W., T. A. Ehlers, S. G. Mitchell, and D. R. Montgomery (2003), Coupled spatial variations in precipitation and long-term erosion rates across the Washington Cascades, *Nature*, *426*(6967), 645–647.
Reneau, S. L., and W. E. Dietrich (1991), Erosion rates in the southern oregon coast range: Evidence for an equilibrium between hillslope erosion and sediment yield, *Earth Surf. Processes Landforms*, *16*(4), 307–322.
Riebe, C. S., J. W. Kirchner, D. E. Granger, and R. C. Finkel (2000), Erosional equilibrium and disequilibrium in the Sierra Nevada, inferred from cosmogenic ^{26}Al and ^{10}Be in alluvial sediment, *Geology*, *28*(9), 803–806.
Roering, J. J., J. W. Kirchner, and W. E. Dietrich (1999), Evidence for nonlinear, diffusive sediment transport on hillslopes and implications for landscape morphology, *Water Resour. Res.*, *35*(3), 853–870, doi:10.1029/1998WR900090.
Schmidt, K. M., J. J. Roering, J. D. Stock, W. E. Dietrich, D. R. Montgomery, and T. Schaub (2001), The variability of root cohesion as an influence on shallow landslide susceptibility in the Oregon Coast Range, *Can. Geotech. J.*, *38*(5), 995–1024.
Seidl, M. A., and W. E. Dietrich (1993), The problem of channel erosion into bedrock, in *Functional Geomorphology*, Catena Suppl., edited by K. H. Schmidt and J. de Ploey, pp. 101–124, Catena Verlag, Cremlingen, Germany.
Shelef, E., and G. E. Hilley (2013), Impact of flow routing on catchment area calculations, slope estimates, and numerical simulations of landscape development, *J. Geophys. Res. Earth Surf.*, *118*, 2105–2123, doi:10.1002/jgrf.20127.

Snyder, N. P., K. X. Whipple, G. E. Tucker, and D. J. Merritts (2000), Landscape response to tectonic forcing: Digital elevation model analysis of stream profiles in the Mendocino triple junction region, northern California, *Geol. Soc. Am. Bull.*, *112*(8), 1250–1263.

Stark, C. P., and N. Hovius (2001), The characterization of landslide size distributions, *Geophys. Res. Lett.*, *28*(6), 1091–1094, doi:10.1029/2000GL008527.

Stock, J. D., and W. E. Dietrich (2003), Valley incision by debris flows: Evidence of a topographic signature, *Water Resour. Res.*, *39*(4), 1089, doi:10.1029/2001WR001057.

Stock, J. D., and D. R. Montgomery (1999), Geologic constraints on bedrock river incision using the stream power law, *J. Geophys. Res.*, *104*(B3), 4983–4993, doi:10.1029/98JB02139.

Takeuchi, A., and P. B. Larson (2005), Oxygen isotope evidence for the late Cenozoic development of an orographic rain shadow in eastern Washington, USA, *Geology*, *33*(4), 313–316.

Tucker, G. E., and R. L. Bras (1998), Hillslope processes, drainage density, and landscape morphology, *Water Resour. Res.*, *34*(10), 2751–2764, doi:10.1029/98WR01474.

Tunnicliffe, J. F., and M. Church (2011), Scale variation of post-glacial sediment yield in Chilliwack Valley, British Columbia, *Earth Surf. Processes Landforms*, *36*(2), 229–243.

Turner, T. R., S. D. Duke, B. R. Fransen, M. L. Reiter, A. J. Kroll, J. W. Ward, J. L. Bach, T. E. Justice, and R. E. Bilby (2010), Landslide densities associated with rainfall, stand age, and topography on forested landscapes, southwestern Washington, USA, *For. Ecol. Manage.*, *259*(12), 2233–2247, doi:10.1016/j.foreco.2010.01.051.

Vaccaro, J. J., M. A. Jones, D. M. Ely, M. E. Keys, T. D. Olsen, W. B. Welch, and S. E. Cox (2009), Hydrogeologic framework of the Yakima River Basin Aquifer System, Washington USGS Scientific Investigations Report 2009–5152.

Vrugt, J. A., H. V. Gupta, W. Bouten, and S. Sorooshian (2003), A Shuffled Complex Evolution Metropolis algorithm for optimization and uncertainty assessment of hydrologic model parameters, *Water Resour. Res.*, *39*(8), 1201, doi:10.1029/2002WR001642.

Wallis, J. R., M. G. Schaefer, B. L. Barker, and G. H. Taylor (2007), Regional precipitation-frequency analysis and spatial mapping for 24-hour and 2-hour durations for Washington State, *Hydrol. Earth Syst. Sci.*, *11*(1), 415–442.

Whipple, K. X. (2001), Fluvial landscape response time: How plausible is steady-state denudation?, *Am. J. Sci.*, *301*, 313–325, doi:10.2475/ajs.301.4-5.313.

Whipple, K. X., and G. E. Tucker (1999), Dynamics of the stream-power river incision model: Implications for height limits of mountain ranges, landscape response timescales, and research needs, *J. Geophys. Res.*, *104*(B8), 17,661–17,674, doi:10.1029/1999JB900120.

Willett, S. D., and M. T. Brandon (2002), On steady states in mountain belts, *Geology*, *30*(2), 175–178.

Yanites, B. J., G. E. Tucker, and R. S. Anderson (2009), Numerical and analytical models of cosmogenic radionuclide dynamics in landslide-dominated drainage basins, *J. Geophys. Res.*, *114*, F01007, doi:10.1029/2008JF001088.